

POLYTECHNIC OF TURIN

**MASTER's Degree in NANOTECHNOLOGIES FOR
ICTS**



MASTER's Degree Thesis

**CHARACTERIZATION OF Zn_3P_2 THIN
FILMS FOR PHOTOVOLTAIC
APPLICATIONS**

Supervisors

Prof. ANNA FONTCUBERTA I MORRAL

Prof. CARLO RICCIARDI

Dr. VALERIO PIAZZA

Dr. RAJRUPA PAUL

Candidate

VANESSA CONTI

OCTOBER 2022

Summary

Zinc phosphide (Zn_3P_2) is a promising earth-abundant material candidate for photovoltaic applications, thanks to its direct band gap, long minority carrier diffusion length and high absorption coefficient. Despite these promising characteristics, there is still lack of knowledge regarding its electrical properties: this hinders the making of a solar cell able to reach the theoretical 30% efficient given by the Shockley–Queisser limit.

The aim of this thesis is to investigate thin films of Zn_3P_2 grown by molecular beam epitaxy by means of different techniques in order to extract the relevant parameters (resistivity, carrier concentration and mobility). The adopted methods involve TLM and C-V profiling along with SIMS analysis.

TLM method is exploited to obtain information about the resistivity of the samples and the contact parameters, as well as the impact of the substrate doping on the electrical transport, while C-V profiling it is employed to find the intrinsic carrier concentration. The acquired data will be correlated with the samples composition obtained from SIMS to understand the impact of the growth parameters on the electrical properties of the material.

Il fosforo di zinco (Zn_3P_2) è un promettente e abbondante materiale, ottimo candidato per applicazioni fotovoltaiche in quanto dispone di band gap diretto, grande lunghezza di diffusione dei portatori minoritari e alto coefficiente di assorbimento. Nonostante queste interessanti caratteristiche, le sue proprietà elettriche non sono ancora ben definite in letteratura: questo ostacola la fabbricazione di una cella solare in grado di raggiungere l'efficienza teorica del 30% data dal limite di Shockley-Queisser.

Lo scopo di questa tesi è investigare film sottili di Zn_3P_2 cresciuti con molecular beam epitaxy attraverso varie tecniche per estrarne i parametri principali (resistività, concentrazione dei portatori, mobilità). I metodi adottati comprendono TLM e C-V profiling, assieme ad analisi SIMS.

Il metodo TLM è sfruttato per ottenere informazioni sulla resistività del materiale e dei parametri di contatto, così come l'impatto del drogaggio del substrato sul

trasporto elettrico, mentre il C-V profiling è impiegato per trovare la concentrazione intrinseca dei portatori. I dati acquisiti saranno poi correlati con la composizione dei campioni ottenuta dalle analisi SIMS per comprendere l'impatto dei parametri di crescita sulle proprietà elettriche del materiale.

Le phosphorure de zinc est un matériau abondant et prometteur pour les applications photovoltaïques en raison de son bandgap direct, sa longueur de diffusion des porteurs minoritaires et le grand coefficient d'absorption. Malgré ses caractéristiques intéressantes, il y a encore un manque de connaissances sur ses propriétés électriques: cela empêche la réalisation d'une cellule solaire dont l'efficacité est capable d'atteindre le maximum de 30% de la limite de Shockley-Queisser.

L'objectif de ce projet de master est d'étudier les films fins de Zn₃P₂ déposés par épitaxie par jet moléculaire avec des techniques différentes pour extraire les paramètres pertinents (résistivité, concentration des porteurs, mobilité). Les méthodes employées sont principalement les mesures TLM et le profiling C-V avec SIMS analyse. Les TLM sont utilisées pour obtenir les informations sur la résistivité des échantillons et les paramètres de contact, ainsi que l'effet du dopage du substrat sur le transport électrique, tandis que le profiling C-V est employé pour trouver la concentration intrinsèque des porteurs. Les informations acquises seront ensuite comparées avec les informations de composition des échantillons obtenus par la SIMS pour comprendre l'impact des paramètres de pousse sur les propriétés électriques du matériau.

Acknowledgements

This is a thing I am really bad at, because expressing how grateful I am towards some people with few words is difficult. Working is not perfectly linear and there can be days when everything seems to be bad, and having someone supporting you it is the best to overcome the difficulties.

First of all, I would like to thank the people in LMSC for the nice time spent together in these months, prof. Anna and Dr. Valerio for their supervision and, last but not the least, my next-door-supervisor Raj that closely followed everything and made less heavy the work even in the more delicate moments. Of course, I cannot avoid to thank also my friends Giacomo and Eleonora for the endless phonecalls we had in this period, and Mr. Ponso, who shared with me the office and a lot of funny moments. A special hug is always dedicated to my mummy, who never stops listening to me complaining.

Besides the thesis, I would like to express my gratitude also to those I met in these two years: people come, people go, but I think all the little moments we spent together are worthy of a mention because they have been all important for one reason or another!

*"See you back in the Universe!"
Vanessa*

Table of Contents

List of Tables	VIII
List of Figures	IX
1 Introduction	1
1.1 A look into zinc phosphide	1
1.2 Electrical characterization of Zn_3P_2	2
2 Methods	3
2.1 TLM measurements	3
2.1.1 Description	3
2.1.2 Structure geometry	5
2.2 CV measurements	6
2.2.1 Schottky diodes	7
2.2.2 Junction capacitance	10
2.2.3 Setup, samples geometry and metal constraints	12
3 Samples	14
3.1 Zn_3P_2 on InP substrate	15
4 Fabrication techniques	17
4.1 Steps description	17
4.1.1 Electron-beam lithography	17
4.1.2 DC sputtering	19
4.1.3 Plasma enhanced chemical vapour deposition	20
4.1.4 Plasma etching	21
4.1.5 E-beam resist and lift-off	22
4.1.6 Focused ion beam	23
4.2 Process flow and structures description	23
4.2.1 Hall and TLM structures process flow	24
4.2.2 CV pads and junction pads process flow	25

4.2.3	Fabricated structures	25
5	Results	27
5.1	TLM measurements	27
5.1.1	Monocrystalline Zn_3P_2 on n-type InP	28
5.1.2	Monocrystalline Zn_3P_2 on p-type InP	31
5.1.3	Polycrystalline and monocrystalline Zn_3P_2 on i-InP	32
5.2	C-V profiling	36
5.2.1	C-V profiling of Schottky diodes	36
5.2.2	C-V profiling of $\text{Zn}_3\text{P}_2/\text{InP}$ junction	42
5.3	I-V curves comparison, threshold and η	45
5.4	SIMS analysis	48
5.5	Mobility	51
6	Conclusions and Outlooks	52
A	Imaging methods	53
A.1	SEM	53
A.2	AFM	54
B	Other results	56
B.1	Zn_3P_2 on graphene and SiO_2 substrate	56
B.1.1	EDX	58
B.2	Zn_3P_2 on InP substrate: Hall measurements and transport	60
B.2.1	Principle	60
B.2.2	Results	63
	Bibliography	66

List of Tables

2.1	Geometrical dimension of the TLM bars.	6
3.1	Samples with InP substrate used during the experiments.	15
5.1	Summary of TLM data from monocrystalline on n-type samples. . .	30
5.2	Summary of TLM data from 04A sample.	34
5.3	Summary of Au contact parameters for monocrystalline zinc phosphide.	35
5.4	Summary of polycrystalline on i-InP data from C-V profiling with Schottky diodes.	40
5.5	Summary of monocrystalline on i-InP and n-InP data from C-V profiling with Schottky diodes.	42
5.6	Summary of data from C-V profiling with the top-bottom approach.	45
5.7	Summary of the ideality factors for the different samples.	47
5.8	Summary of data from C-V profiling with the top-bottom approach.	48
5.9	Summary of data extracted from SIMS analysis.	49
5.10	Summary of mobility values.	51
B.1	Table showing the Zn/P for the different Zn_3P_2 on graphene samples.	59

List of Figures

2.1	Simple geometrical model of a semiconductor with its main geometrical parameters.	4
2.2	Schematic of the contact parameter showing the transfer length and the contact extension Δx	4
2.3	Example of a TLM structure. The distance between the contacts is increasing with the length.	5
2.4	The TLM structure geometries used for the characterization.	6
2.5	Schematic showing the electrical and the depletion capacitance.	8
2.6	Schematic showing an equivalent circuit for the semiconductors interface, modeling it as a passive network considering a negligible voltage bias at the junction.	9
2.7	Equivalent circuit showing the effect of the series resistance on voltages and currents.	9
2.8	Equivalent circuit for the effect of the series resistance.	10
2.9	Total capacitance for Schottky and semiconductor junctions in series.	11
2.10	Layout of the C-V pads for Schottky diode configuration.	12
2.11	Band diagrams for separated (left) and attached (right) metal and Zn_3P_2	13
3.1	Cross section of a monocrystalline sample showing a deep crack. In the small square cracks on the surface and its rugosity can be observed.	16
4.1	Schematic of an e-beam column.	18
4.2	Fracturing process to convert from .gds to .gpf.	18
4.3	Zoom of a gold alignment marker.	19
4.4	Sputtering schematic	20
4.5	PECVD schematic.	21
4.6	Plasma etching chamber schematic.	22
4.7	Lift off process	23
4.8	TLM structure version A (left) and B (right).	26
4.9	C-V pads (a) and Hall bar (b) structures.	26

5.1	Resistance versus length for monocrystalline on n-type InP samples. Black markers show the acquired data.	28
5.2	Different current paths depending on the length.	29
5.3	Example of I-V curves for 17B sample. The curves are ohmic for small distances and then they become Schottky. The picture reports the behaviour until L_{crit} and for the maximum distance ($480 \mu m$).	29
5.4	Band alignment for Zn_3P_2 (right) and n-InP (left). Zinc phosphide carrier concentration was set to $10^{15} cm^{-3}$	30
5.5	Band alignment for InP (left in the graph) and Zn_3P_2 (right in the graph). The thickness of the region featuring barriers at the interface is about 80-50 nm, while the barrier height is 0.2-0.1 eV, depending on the chosen carrier concentration.	31
5.6	TLM graph (left) clearly shows the scattered behaviour, while the I-V curves (right) remain perfectly ohmic for a large distance range.	32
5.7	TLM graphs for polycrystalline samples with different metal contacts.	33
5.8	Example of I-V curves for 04C (Au) sample. The curves are slightly noisy, but ohmic.	33
5.9	TLM graph and I-V curves for monocrystalline sample (04A) on intrinsic indium phosphide substrate.	34
5.10	Band alignment for Zn_3P_2 (right) and i-InP (left). Zinc phosphide carrier concentration was set to $10^{15} cm^{-3}$	35
5.11	I-V comparison for Al, Cr, Ti.	37
5.12	C-V comparison for Al, Cr, Ti.	37
5.13	Intersection points with the voltage axis for monocrystalline Zn_3P_2 on n-InP. The values have been normalized with respect to the first point.	38
5.14	Some interpolation lines for sample V1-19-04-06-B extracted for different pad distances and metal. The graphs report the registered variation coefficient between the lines and the computed carrier concentration.	39
5.15	Comparison between two polycrystalline on intrinsic substrate (V1-19-10-29-A, V1-19-04-06-B) for Cr and Al contacts.	39
5.16	04-04-C comparison with 04-06-B showing a similar carrier concentration (a). A focus on the variation coefficient of 04-04-C (b).	40
5.17	C-V profiling for monocrystalline samples 17A (a) V1-02-11-A (b).	41
5.18	I-V curves and C-V profiling for two pieces of V1-19-04-06-B (polycrystalline on i-InP).	42
5.19	C-V profiling for V1-19-04-04-C (polycrystalline on intrinsic InP).	43
5.20	I-V and C-V curves for V1-19-02-11-A (monocrystalline on i-InP).	44
5.21	C-V profiling for two pieces of V1-19-04-04-A (monocrystalline on intrinsic InP).	44

5.22	I-V in linear scale.	45
5.23	I-V in semilog scale.	46
5.24	Ideality factor vs Voltage.	46
5.25	I-V and ideality factor curves for 17A and 17B (monocrystalline on n-InP).	47
5.26	Carrier concentration versus Zn/P ratio.	49
5.27	C-V profiling for 17B.	50
A.1	SEM schematic.	53
A.2	AFM schematic.	55
B.1	SEM pictures showing the flakes on the surface (left) and its zoom (right). The dimension of the smaller features is in the range of 100 nm.	57
B.2	Surface of three different graphene samples.	57
B.3	AFM picture of the sample surface. The presence of isolated triangular flakes is evident.	58
B.4	Composition of the graphene samples in atomic%.	58
B.5	Zn/P atomic ratio vs gas flux ratio (V/II) in the chamber (left) and growth temperature (right).	59
B.6	Appearing of V_H in a p-type semiconductor.	61
B.7	Structure of a Hall bar showing the current injection and the terminal where the resistances R_{yx} and R_{xx} are sensed.	62
B.8	Resistance versus temperature on the longitudinal channel for a monocrystalline on p-InP.	63
B.9	Natural logarithm of R_{xx} vs $1/T$	64
B.10	Parabolic behavior of R_{xx} with the magnetic field.	65

Chapter 1

Introduction

1.1 A look into zinc phosphide

Solar power is the predominant source of energy on the planet among the renewable ones available. Despite the growing demand for this technology, there is still need to diversify the market, developing stable, efficient and cheap commercial devices. One of the most promising candidates to fill this gap is zinc phosphide.

Zinc phosphide (Zn_2P_3) is an earth-abundant semiconductor, showing interesting optoelectronics properties, such as a high absorption coefficient ($\sim 10^4 - 10^5 \text{ cm}^{-1}$) for the visible spectrum, a long minority-carriers diffusion length ($\sim 10 \mu\text{m}$) and a direct bandgap of $\sim 1.5 \text{ eV}$, close to the optimum of the Shockley–Queisser limit leading to a theoretical efficiency higher than 30% [1].

Besides these advantages, there are some technological challenges to overcome in order to successfully exploit zinc phosphide as a solar cell material: for example, it exhibits a large cell dimension with tetragonal structure at room temperature [2] and a large thermal expansion coefficient [3], which promote the formation of structural defects during the growth or after, upon cooling the material. For what concerns the growth, the principal methods are related to molecular beam epitaxy (MBE) and chemical vapor deposition (CVD) techniques [4] or their variants (ex. selective MBE, van der Walls epitaxy, metal-organic CVD [5]). Growth can be performed on different substrates, such as InP or GaAs [6], thanks to their small lattice mismatch with Zn_3P_2 , or mica and silicon steel, which exhibit similar thermal expansion coefficients with respect to the zinc phosphide one [7].

1.2 Electrical characterization of Zn_3P_2

Zinc phosphide crystal structure favors the formation of defects such as zinc vacancies and phosphorus interstitials [8]. The latter are the most favorable to be formed due to the small energy demand and they act as electrons sink, neutralizing the effect of the donor atoms [9]. Therefore epitaxially grown Zn_3P_2 tends to be intrinsically p-doped and it is difficult to achieve a good n-type doping level. Despite this process, known as self-compensation, there are some atomic species which have been found to be efficient donors: Al, Ga, In in Zn-rich conditions. Concerning the case of extrinsic p-type doping, Na and Cu act as good acceptors [10]. The lack of n-type Zn_3P_2 is one of the obstacles towards the engineering of a p-n junction based single junction solar cell. For this reason, other strategies have been explored so far. The best solar cell ever realized with zinc phosphide exploits Mg to create a Schottky diode: this architecture eliminates the need to have a n-type semi-junction, but it does not exploit the full potentiality of Zn_3P_2 , limiting the efficiency to an actual maximum of 5.96% [11].

To make an efficient electric device, also resistivity and mobility are important as well. For zinc phosphide room temperature electric mobility has been reported to be in a large interval values, ranging from 10-20 $\frac{\text{cm}^2}{\text{Vs}}$ to even 310 $\frac{\text{cm}^2}{\text{Vs}}$, especially depending on the crystallinity state of the sample (monocrystalline or polycrystalline) [12][13]. Naturally, also the resistivity is impacted by the crystallinity grade and the doping: intrinsic polycrystalline Zn_3P_2 seems to generally exhibit quite high values, hitting also $10^6 \Omega \cdot \text{cm}$ [14]. For p-type polycrystalline layers, lower values around $10^2 \Omega \cdot \text{cm}$ have been reported as one can expect [15]. Due to the absence of grain boundaries, monocrystalline samples show a lower resistivity, with reported values of even $250 \Omega \cdot \text{cm}$ for intrinsic samples [16]. Annealing in phosphorus atmosphere has been demonstrated to be a good method to reduce the resistivity of intrinsic zinc phosphide crystals (carrier concentration of $10^{13} - 10^{14} \text{ cm}^{-3}$) from $10^4 - 10^6 \Omega \cdot \text{cm}$ to $10^3 \Omega \cdot \text{cm}$ [17] thanks to the higher number of phosphorus interstitials. Unfortunately, despite researchers have been working on zinc phosphide for about 40 years, there is still a lack of literature and great variability about its fundamentals properties, especially on the ones related to electric transport, which hinders the possibility to successfully exploit Zn_3P_2 as an efficient solar cell material. The aim of this work is to investigate some of these properties, mainly resistivity and mobility, by means of different techniques, along with methods to extract the carrier concentration from the available samples. Samples and methods will be described in the following sections before to show the relevant results.

Chapter 2

Methods

In this chapter the main measurements methods used to investigate resistivity and hole mobility in Zn_3P_2 will be described: the working principle will be elucidated and the fundamental equations used for the data analysis will be presented. Additional methods used to investigate the samples (SEM, AFM) discussed in this thesis are reported in the Appendix.

2.1 TLM measurements

Transfer length measurements (TLM) is a 2-probe technique used to extract information related to the quality of the formed contact between a deposited metal and the underlying material. Moreover, it can be used to extract the material resistivity. In the following subsection a brief introduction to the theory behind the method will be given [18].

2.1.1 Description

Considering a piece of semiconductor as the one shown in fig. B.7, the total measured resistance R_{tot} is given by the sum of the metal resistance R_m , the semiconductor resistance R_s and the resistance of the contact R_c :

$$R_{tot} = 2R_m + R_s + 2R_c \quad (2.1)$$

The metal resistance is usually much smaller than the semiconductor and the contact resistance, so in the following analysis it will be neglected.

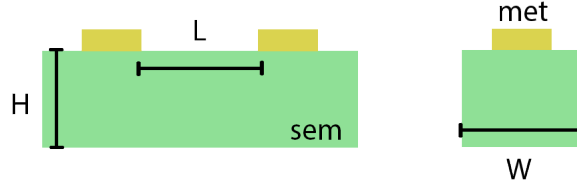


Figure 2.1: Simple geometrical model of a semiconductor with its main geometrical parameters.

Concerning the semiconductor resistance, it can be expressed in function of the resistivity ρ_s and the geometrical parameters of the piece:

$$R_s = \rho_s \frac{L}{WH} = R_{sh} \frac{L}{W} \quad (2.2)$$

Where L , W and H are respectively the length, the width and the thickness of the piece. R_{sh} is defined as the sheet resistance. The contact resistance is instead function of the contact area A_c and the contact resistivity ρ_c :

$$R_c = \frac{\rho_c}{A_c} = \lim_{\Delta x \rightarrow 0} \frac{\rho' \Delta x}{A_c} \quad (2.3)$$

The contact resistivity is defined as the equivalent resistivity ρ' of the portion Δx between the metal and the semiconductor, where Δx is ideally limited to the interface, being almost null. Concerning A_c , it usually does not match the physical contact area: depending on the electric field lines, carriers tend to be accumulated in a small portion of the contact, whose geometric dimensions are the width W and the transfer length L_T , the average distance before carriers flow in the contact itself. Picture 2.2 visually describes the phenomenon.

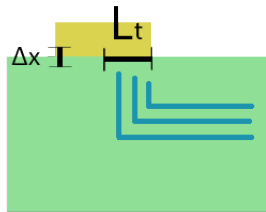


Figure 2.2: Schematic of the contact parameter showing the transfer length and the contact extension Δx .

Expressing the contact in function of its geometrical parameters, the resistance created at the semiconductor interface can be expressed similarly to eq. 2.2, with

L_T as the effective distance. Substituting all the terms in 2.1, the total resistance becomes function of the length:

$$R_{tot} \sim R_s + 2R_c = \frac{R_{sh}}{W}(L + 2L_T) \quad (2.4)$$

Knowing the geometrical parameters, one can plot the resistance for different length values and extracting the sheet resistance and the resistivity from the slope, the transfer length and the contact resistance from the interception of the interpolation line with the x and y axis. Once the transfer length is known, by means of equation 2.3 the specific contact resistivity can be found:

$$L_T = \sqrt{\frac{\rho_c}{R_{sh}}} \quad (2.5)$$

2.1.2 Structure geometry

To do TLM measurements, the structure must have metal pads acting as electrical contacts and placed at different distances. To obtain the resistance value, a probe station is used to apply a voltage and to sense the current between a couple of pads. All around the structure an insulating material could be deposited to avoid unwanted dispersion of the field lines. Figure 2.3 shows an example of a possible TLM structure. For adjacent contacts the distance L_i is computed regardless to the contact dimension, considering the transfer length negligible with respect to the path in the semiconductor.

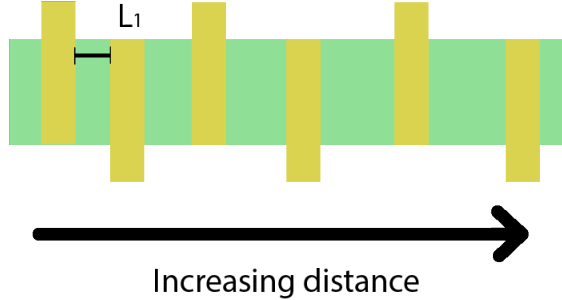


Figure 2.3: Example of a TLM structure. The distance between the contacts is increasing with the length.

Geometry has an impact on the uncertainty of the derived values. It can be demonstrated that it exists an optimum width value of the TLM bar to reduce the systematic error in the measurement of the contact resistivity: since the error on ρ_c directly depends on R_{sh} and W values, one can choose the width to minimize

this error. It means that the optimum width can be computed starting from an estimation of the sheet resistance and the contact resistivity itself [19].

In the following characterization geometries similar to the one in the previous figure have been adopted, using different kind of metals as contacts (Au, Ag, Zn-Au) and sometimes isolating the structure with silicon nitride.

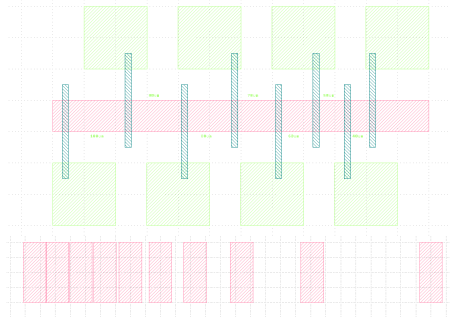


Figure 2.4: The TLM structure geometries used for the characterization.

The simpler structure adopted in fig. 2.4 (bottom one) was used on some of the last monocrystalline samples processed in order to reduce the fabrication steps to only one e-beam lithography step, trying to avoid cracks propagation in the zinc phosphide layer. More information about the full process of the bars can be found in the inherent section.

Concerning the geometrical dimensions, table 2.1 summarizes the data of the top structure (A) and the bottom structure (B).

structure	length range [μm]	width [μm]	thickness [μm]	contact length [μm]
A	30-480	50	1	10
B	10-1010	200/300	1	75

Table 2.1: Geometrical dimension of the TLM bars.

All the measurements have been taken with a probe station using a Keithley analyzer and a LabVIEW interface. The voltage sweep range is always between -500 mV and 500 mV.

2.2 CV measurements

CV measurements are a common type of measure to extract the carrier concentration of a semiconductor and to have a quantification of the built-in potential V_{BIN} in a diode. There are different variants of the method depending on the kind of structure

that is used, whether it is a Schottky diode, a MOS structure, a metal-insulator diode or a junction between different semiconductors. Regardless the structure, the main point is to sweep across the DC voltage, meantime applying an AC signal of a certain frequency and amplitude [20].

2.2.1 Schottky diodes

A Schottky diode is a diode between a semiconductor and a metal forming a Schottky contact with the semiconductor itself. In order to create a Schottky contact, a depletion region must be present at the interface between the two materials: this is translated into a constrain on the metal workfunction [21]. More details about the metal constraint will be given in the following.

Concerning the capacitance C_d , once a depleted region of extension x_d is formed, its expression can be approximated as the one of a parallel-plates capacitor, being x_d the distance between the plates (metal and non-depleted region):

$$C_d = \frac{\epsilon A}{x_d} \quad (2.6)$$

Modelling the charge accumulation in the metal as a δ -Dirac function and considering the semiconductor homogeneously depleted in the region x_d , applying the neutrality condition one finds from Poisson equations the expression of the depletion region. Considering to apply a positive voltage on the semiconductor side, its expression for a p-type semiconductor is dependent on the total voltage drop across the junction and the carrier concentration N_A :

$$x_d = \sqrt{\frac{2\epsilon}{qN_A}(V_{BIN} - V)} \quad (2.7)$$

This means that the depletion capacitance can be expressed as a function of the carrier concentration. In particular, it is interesting to plot $\frac{1}{C_d^2}$ with respect to the applied voltage, since combining expressions 2.6 and 2.7 the carrier concentration can be directly extracted from the slope while the sign of the slope gives information about the type of majority carriers present in the material:

$$\frac{1}{C_d^2} = \frac{2}{A^2 q \epsilon N_A} (V_{BIN} - V) \quad (2.8)$$

Besides the simplicity of the method, there are some parasitic effects to take into account. The main two are related to the presence of parasitic capacitance and the series resistance effect.

Parasitic capacitance

There are several elements that could give contributions to the total measured capacitance, such as cables, parasitic junction capacitance and electrical capacitance between pads. Considering the setup optimized to filter all the effects related to the tool, in the following a brief description of the junction and electrical capacitance will be given.

The electric capacitance C_{el} is a parasitic capacitance that could couple to the system when more pads are placed together on the same plane. As shown in fig. 2.5, it can be modelled as a parallel plate capacitance, where the area is the lateral pad area A_{pad} and the distance is the pad spacing s between the pads:

$$C_{el} = \frac{\epsilon_{air} A_{pad}}{s} \quad (2.9)$$

Which gives a fast estimation of its value. In the case of a planar configuration (fig.2.5), the total capacitance can be seen as the parallel of the electric and the depletion capacitance. Considering C_{el} independent from the bias, its effect can be neglected when extracting the slope. Nonetheless, it affects the frequency behavior of the total capacitance. More details will be provided in the following.

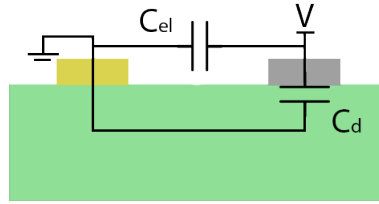


Figure 2.5: Schematic showing the electrical and the depletion capacitance.

Concerning the junction capacitance C_j , it can become an important factor to take into account when the material is grown on another semiconductor, as in the case here described: a junction is made between the top and bottom semiconductors, creating a capacitance at the interface. This capacitance has an effect on the total measured one, so it could be useful to try to analyze it: one can consider the case of in-plane couples of pads, where one of the pad is Schottky and the other one is ohmic. In fig. 2.6 an equivalent electrical model is proposed.

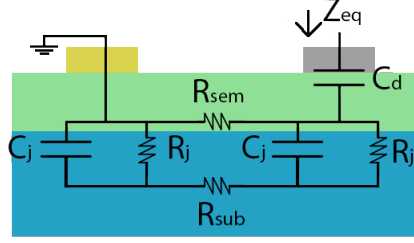


Figure 2.6: Schematic showing an equivalent circuit for the semiconductors interface, modeling it as a passive network considering a negligible voltage bias at the junction.

One can define R_{sem} as the resistance of the semiconductor material to characterize, while R_{sub} and R_j are respectively the substrate resistance and the equivalent resistance carriers see to cross the junction between the material and the substrate. The total equivalent impedance Z_{eq} measured at the Schottky terminal is given by a complex expression:

$$Z_{eq} = \frac{1}{sC_d} \frac{As^2 + Bs + 1}{1 + Ds} \doteq \frac{1}{sC_d} \times A(s) \quad (2.10)$$

Where A , B and D are dependent on the capacitance and the resistances in the equivalent circuit. The equivalent capacitance which can be measured from the terminal can be expressed as a function of the equivalent impedance considering its modulus. Equation 2.11 shows that it is equal to C_d multiplied by a term whose amplitude is varying in frequency:

$$C_{eq} = \frac{1}{\omega |Z_{eq}|} = C_d \times B(\omega) \quad (2.11)$$

Series resistance

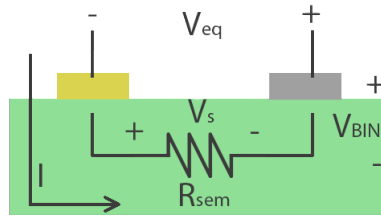


Figure 2.7: Equivalent circuit showing the effect of the series resistance on voltages and currents.

The series resistance R_{sem} is the resistance offered by the semiconductor. It is the source of several inaccuracy in the measure. Considering the schematic in figure 2.7, the equivalent voltage V_{eq} between the contacts can be expressed in function of the voltage drop on the semiconductor:

$$V_{eq} = V_{BIN} - IR_{sem} \quad (2.12)$$

This means that V_{eq} cannot approach V_{BIN} . As a consequence, closer to the point $V \sim V_{BIN}$ when sweeping on the voltage on a CV measurement, the line won't intersect the point $\frac{1}{C_d^2} = 0$ due to the impossibility to have $V = V_{eq} = V_{BIN}$ in equation 2.8.

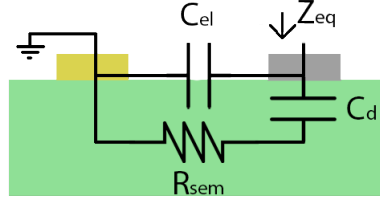


Figure 2.8: Equivalent circuit for the effect of the series resistance.

An other effect of the series resistance is the frequency modulation of the total capacitance amplitude. Given the schematics in fig. 2.8, the equivalent capacitance can be expressed as a function of the equivalent impedance seen similarly to eq. 2.11:

$$C_{eq} = \frac{1}{\omega|Z_{eq}|} = (C_{el} + C_j) \times \sqrt{\frac{1 + (\omega C_s R_s)^2}{1 + (\omega C_d R_s)^2}} \quad (2.13)$$

Where C_s is the series between C_d and C_{el} . Considering $C_{el} \ll C_d$ one can approximate the transfer function as a single pole function. Since the measurements are done with an applied AC signal, these effects and the one caused by the junction capacitance in eq. 2.11 are important to determine what's the optimal frequency value to maximize the signal-to-noise ratio.

2.2.2 Junction capacitance

In the previous paragraphs the junction capacitance C_j has been presented as a parasitic element. Nonetheless, it still contains information about the carrier concentration of the material. Considering a general p-n heterojunction with a bias V applied to the p-side, it can be found [22] that the junction capacitance is

equivalent to:

$$C_j = A_j \sqrt{\frac{q\epsilon_{Zn_3P_2}\epsilon_{InP}N_{Zn_3P_2}N_{Zn_3P_2}}{2(\epsilon_{Zn_3P_2}N_{Zn_3P_2} + \epsilon_{InP}N_{InP})}} \times \sqrt{V_{BIN} - V} \quad (2.14)$$

Reversing the formula one can obtain the carrier concentration.

It can happen that the contact placed on the zinc phosphide surface is not perfectly ohmic for some reasons (process conditions, pinning of the Fermi level...). In the case where the area of the contact A_c is similar to the area of the junction A_j (e.g. contact covering all the chip), the junction behaviour can be "masked" by a Schottky one.

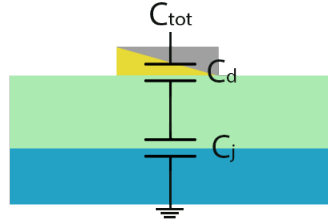


Figure 2.9: Total capacitance for Schottky and semiconductor junctions in series.

When a mixed behaviour is present, the total capacitance C_{tot} is given by the series between C_d and C_j . Considering $A_c = \alpha A_j$, one can derive the carrier concentration in the zinc phosphide as:

$$N_1 = \text{mod} \frac{-2(\gamma - \alpha^2\beta)\epsilon_2 N_2}{2\alpha^2\beta\epsilon_1 - \frac{\Delta \frac{1}{C_{tot}^2}}{\Delta V} \epsilon_1 \epsilon_2 q A_c^2} \quad (2.15)$$

Where the nomenclature "1" is referring to Zn₃P₂ and "2" to InP to make less heavy the notation. The terms γ and β are two parameters modeling the different voltage drop across the two junctions: these are unknown elements, therefore is only possible to obtain a rough estimation on N_1 making assumptions on their values.

The kind of structure used for these C-V measurements is also useful to sense the current across the junction between Zn₃P₂ and InP. Plotting the I-V curves in semilog scale, one can extract the diode threshold and the ideality factor. Reversing the current expression and extracting the slope m of the linear part in the forward region one finds:

$$\eta = \frac{1}{mk_B T} \times \frac{1}{\log 10} \quad (2.16)$$

2.2.3 Setup, samples geometry and metal constraints

For the setup of the C-V measurement a probe station Keithley was used. Concerning the geometry and the metal, to realize Schottky diodes series of couples of ohmic and Schottky contacts placed at different distances have been placed. Initially this kind of configuration was adopted also for the junction capacitance measure, stacking the chip on a piece of gold-covered wafer and contacting the ohmic contact and the underneath wafer. Fig. 2.10 shows the layout.

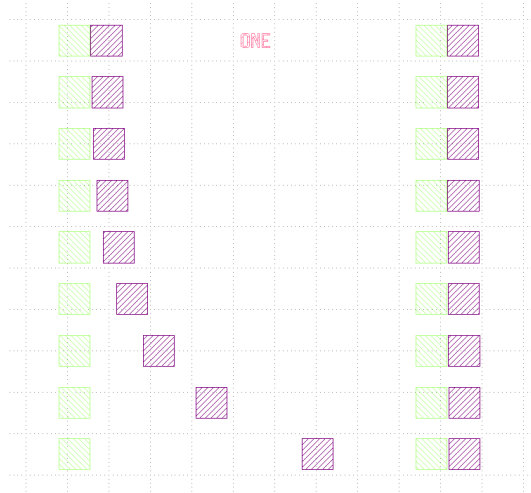


Figure 2.10: Layout of the C-V pads for Schottky diode configuration.

The dimension of the pads is $150\mu m \times 150\mu m$, while their thickness is different depending on the kind of metal used. More details about the fabrication process will be given in the next sections. Concerning the metal, to form a Schottky contact a constraint on the metal workfunction must be respected: a depletion region must be created at the semiconductor interface with the metal. This means that the Fermi level of the metal should be higher in energy than the one of the semiconductor in the case of a p-type one, as it is for zinc phosphide. In picture 2.11 a schematic of a band diagram between a p-type semiconductor and a metal shows visually the constraint to respect:

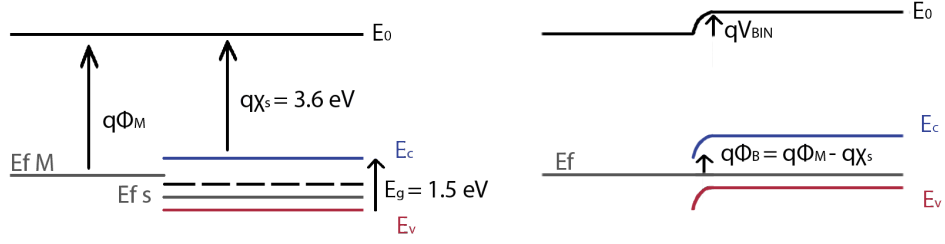


Figure 2.11: Band diagrams for separated (left) and attached (right) metal and Zn_3P_2 .

The difference between the valence band level and the Fermi level can be expressed in function of the holes concentration p in the semiconductor and the equivalent density of states for the holes N_v . This leads to a simply relation between the semiconductor affinity $q\chi_s$, its bandagap E_g , the term depending on the holes concentration and the metal workfunction:

$$q\phi_m < q\chi_s + E_g - (E_{f_s} - E_v) = q\chi_s + E_g + k_B T \ln \frac{p}{N_v} \quad (2.17)$$

Which for a perfect intrinsic Zn_3P_2 is translated into $q\phi_m < 4.35$ eV, being $q\chi_s = 3.6$ eV and $E_g = 1.5$ eV [23]. As it can be graphically observed from pic 2.11, the difference between the metal workfunction and the electric affinity gives the value of the barrier height $q\phi_B$. Actually, it was demonstrated [24] that the barrier height is also dependent on the released energy during the contact formation more than on the metal workfunction. The barrier height $q\phi_B$ defines the amount of current the diode is able to give, hence the signal-to-noise ratio and the quality of the measurements:

$$I = A_R T^2 A e^{-\frac{q\phi_B}{kT}} \left(e^{\frac{V}{\eta V_t}} - 1 \right) \quad (2.18)$$

Where A is the junction area, A_R is the Richardson constant, V_t is the thermal voltage and η is the ideality factor of the diode. Since the leakage current is an important source of error in C-V measurements [25], a suitable control of the barrier could lead to more accurate results.

The depletion region has an extension depending on the carrier concentration of the material. Lower is the carrier concentration and larger will be the depleted region. Given the Schottky metal and the InP parameters, one can compute the minimum carrier concentration which leads to x_d close to the Zn_3P_2 thickness. Using built-in potential values extracted from COMSOL Multiphysics for the different barriers, one finds $N_{min} \sim 10^{12} \text{ cm}^{-3}$ for both Schottky and InP junctions.

Chapter 3

Samples

The study was conducted on two different types of samples: in the first case Zn_3P_2 was grown on indium phosphide (InP) as substrate material; in the second case the material was grown on a substrate made of a graphene layer attached to bulk silicon oxide. The samples characteristics, such as topography and the percentage of zinc phosphide coverage on the surface, are different. In particular, the samples with graphene has found to exhibit a poor film coverage, therefore the electrical characterization was performed with the samples grown on InP, despite the conductive substrate. Information about these samples can be found in the Appendix.

Both the sample typologies have been grown using a molecular beam epitaxy (MBE) system. Epitaxy is a deposition technique performed in reactors whose environment is under ultra-high-vacuum (UHV) condition. UHV is needed to minimize the contamination and improve the layer quality. Also, it allows the MBE growth to happen in the so called molecular regime: in the molecular regime atoms and molecule do not collide thanks to a mean free path between collision higher than the physical dimensions of the chamber. This allows high film quality and the possibility to abruptly change the composition, thanks to reactivity of the shutter system (~ 0.1 s) with respect to the deposition rate in UHV ($\text{\AA}/s$).

The thin layers are grown on a substrate which is heated up to generally 500-700 °C to allow the adsorbed species to diffuse on the surface, forming an ordered lattice. In fact, epitaxy is a technique allowing a maximum lattice mismatch around 10% between the substrate and the grown layer. The material to deposit is generally evaporated in Knudsen cells or supplied in gas form [26].

3.1 Zn₃P₂ on InP substrate

In this paragraph the Zn₃P₂ thin films grown on InP substrate are described. They show a zinc phosphide layer of 0.8-1 μm of thickness on a 325 μm indium phosphide layer with 100 crystallographic orientation. Beside the standard unit cell mismatch between InP and Zn₃P₂ is about 27%, InP is a suitable substrate for epitaxial growth due to the possibility to exploit phosphorus sub-lattice overlapping, which leads the lattice mismatch between Zn₃P₂ and its InP to only 2.3% [27].

Samples have been grown in Laboratory of Semiconductor Materials (LMSC) at the École polytechnique fédérale de Lausanne (EPFL) by M. Zamani. in 2019 using a Veeco GENxplor MBE system. The procedure consists into exposing the substrate to P (V) and Zn (II) gasses with a variable ratio between the two fluxes (V/II ratio). A stoichiometric growth was achieved for fluxes ratio between 0.48 and 0.83, but most of the samples of interest for the electrical studies are characterized by a V/II = 0.72 growing condition. Before to start the effective growing, substrate has been subjected to a degassing step of 2h at 150 °C, followed by another degassing step of 2h at 300 °C. Finally, a last degassing step has been done for 10 minutes at 580 °C with a pressure of 10⁻⁴ Torr to remove the native oxide layer allowing zinc phosphide growth [28].

Table 3.1 reports info about the crystallinity (polycrystalline and monocrystalline Zn₃P₂) and the doping type of the substrate (n-type, intrinsic or p-type InP) of all the samples used for the following experiments. The name is made up by "V1" (reactor used for the growth) and its growing date, along with a letter indicating the order of the growth for samples grown on the same day.

Substrate doping ⇒ Film type ↓	n-type	intrinsic	p-type
polycrystalline	-	V1-19-04-06B	-
	-	V1-19-10-29A	-
	-	V1-19-04-04C	-
monocrystalline	V1-19-12-17A	V1-19-04-04A	V1-19-05-06C
	V1-19-12-17B	V1-19-02-11A	-
	V1-19-12-17C	-	-

Table 3.1: Samples with InP substrate used during the experiments.

Concerning the sample morphology, grown Zn₃P₂ appears as a homogeneous thin film. Figures 3.1 shows a view of the surface and a cross-section image. During the growing time, zinc phosphide nuclei evolves in nano-pyramids, which are able to create a homogeneous thin film structure once they coalesce one with the other, leading to a 001 zinc phosphide surface orientation [29].

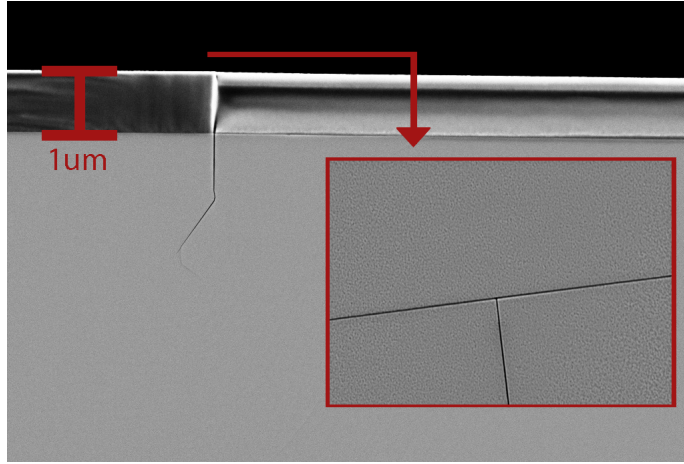


Figure 3.1: Cross section of a monocrystalline sample showing a deep crack. In the small square cracks on the surface and its rugosity can be observed.

Despite the uniform coverage, monocrystalline samples surface is characterized by the presence of cracks. Cracks alter the propagation of the current, which could pass through the substrate in the case of a deep crack cutting along the entire thickness of the zinc phosphide layer. To avoid this possibility, the fabrication of test structures was planned to keep the devices far from the cracks. More details will be given in the related section.

The origin of the cracks is related to the heating of the substrate during Zn_3P_2 growth, and the subsequent cooling down. In fact, InP has a thermal expansion coefficient of about $4.5 \times 10^{-6} \text{ }^\circ\text{C}^{-1}$ [30], while Zn_3P_2 one is $14 \times 10^{-6} \text{ }^\circ\text{C}^{-1}$ [31]: the large mismatch induces a stress during the cooling, and as a consequence the generation of cracks after relaxation.

Chapter 4

Fabrication techniques

The analysis of the electrical properties of the epitaxially grown thin films required the fabrication of test structures. This chapter describes the process flow used to obtain device-like structures from the bare semiconductor. Fabrication of characterization structures has been done in the Center of MicroNanoTechnology (CMi) of the EPFL campus. One notices that due to common steps also Hall bars fabrication is reported, although the discussion of these results is in the Appendix.

4.1 Steps description

The fabrication steps mainly involve e-beam lithography to pattern the metal contacts and the shape of the test structures on the surface, which has been usually covered with silicon nitride to guarantee a good electrical isolation. Metal contacts have been deposited with DC sputtering, while silicon nitride has been etched with a plasma etching system.

The usage of e-beam lithography is determined by the need to place test structures far from the cracks in monocrystalline samples: being e-beam lithography a maskless technique, this is possible simply moving a digital mask on the desired surface location. Concerning the metal deposition, DC sputtering machine was adopted to achieve a conformal deposition of a wide range of metals not heating the surface, which could cause the dangerous possibility of phosphorus atoms releasing. All the details related to each step will be presented in the following subsections.

4.1.1 Electron-beam lithography

E-beam is a maskless lithography method allowing the drawing of a pattern (layout) on a resist surface. The resist is a polymer sensible to the action of the incident ray and after exposure and development in a specific solution it can be dissolved

(positive resist) or it can crosslink (negative resist) to show the layout on the surface. Depending on the dose (amount of electrons on the surface), the chosen current and the relative beam spot size, resolution in the range of nm or even less can be achieved. [32] [33]

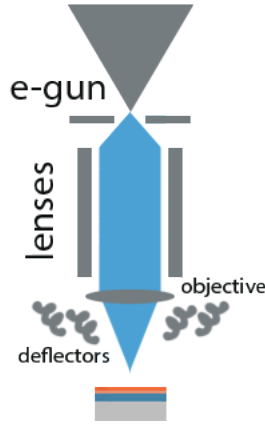


Figure 4.1: Schematic of an e-beam column.

Electron beam is generated by means of an electron gun. The CMi tool (Raith EBPG5000) exploits a thermal field emission gun working at 100 keV [34]. This kind of electron gun is made by a metallic filament which is heated and subjected to a strong electric field providing a really stable current across time [35]. After generation, the e-beam passes through several electrostatic and electromagnetic lenses to control the spot size and it is deflected to reproduce the pattern on the surface. Finally, it is condensed by an objective lens on the point to expose [36].

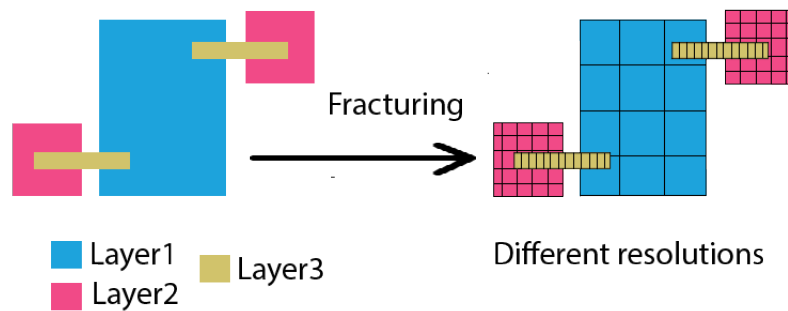


Figure 4.2: Fracturing process to convert from .gds to .gpf.

Being a maskless lithography technique, the pattern is drawn exploiting a virtual mask. One starts from a .gds file containing the layout data (e.g. the geometrical

shapes to reproduce on the surface), then the layout is divided in small rectangles (fracturing) whose dimension gives the resolution that the beam size should match and a .gpf file is produced. Finally, depending on the machine and the desired dimension of the spot, dose and current can be chosen.

Concerning the e-beam steps done in this work, beam currents used are starting from the minimum value (0.1 nA , resolution 5 nm) to higher ones depending of the critical dimension of the features. Dose was set to $800 \frac{\mu\text{C}}{\text{cm}^2}$ to reduce the risk of features overlapping (over-exposure). The choice of the dose is depending on the critical dimension and the adopted resist.

To fabricate the characterization structures, subsequent e-beam steps have been done. When more steps have to be done on the same sample there is the need to fabricate alignment markers, which are able to give to the machine a spatial reference for the following exposures: when the beam is scanned on alignment markers, a contrast is produced with respect to the surface scanning and this allows the tool to recognize their presence [37]. Alignment markers can be of different size and shapes and they can be made depositing heavy metals (e.g. $100\text{-}150 \text{ nm}$) creating an area with high atomic number or etching sufficiently deep the surface. In this work a combination of platinum (10 nm) and gold (100 nm) is used for their realization.

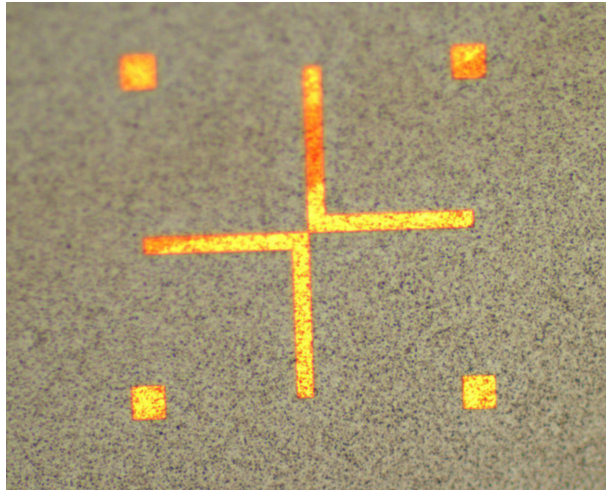


Figure 4.3: Zoom of a gold alignment marker.

4.1.2 DC sputtering

Sputtering is a physical vapour deposition technique in which the material to deposit is extracted from the source (target) by bombarding it with ions in a chamber filled with an inert gas in plasma form. The target works as cathode while

the substrate material as anode. The applied voltage can be a DC one or a RF one. RF voltage is usually adopted in order to deposit dielectric material. Since in this work sputtering was used for metal contacts and alignment markers, the system was configured with a DC voltage. Other elements that can be present are the magnetrons, vacuum tube which confine the plasma near to the target thanks to generation of strong electro-magnetic fields [38].

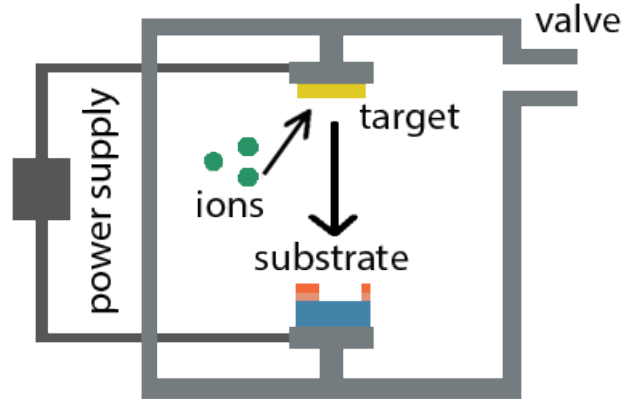


Figure 4.4: Sputtering schematic

CMi tool (Alliance-Concept DP 650) is able to perform deposition at room temperature and high temperature (max. 400 °C). In the case of this work only room temperature depositions have been performed. Moreover, before the deposition, treatments with Ar have been done to mill the native oxide from the surface.

4.1.3 Plasma enhanced chemical vapour deposition

Plasma enhanced chemical vapour deposition (PECVD) is a deposition method where plasma is exploited in order to decrease the temperature deposition. Plasma is created by means of a RF generator and it enhances the formation of reactive species starting from a precursor gas, enhancing the deposition rate of the film on the surface: the substrate is usually placed between two electrodes where the RF signal is applied and during the process is moderately heated to favour the reaction [39].

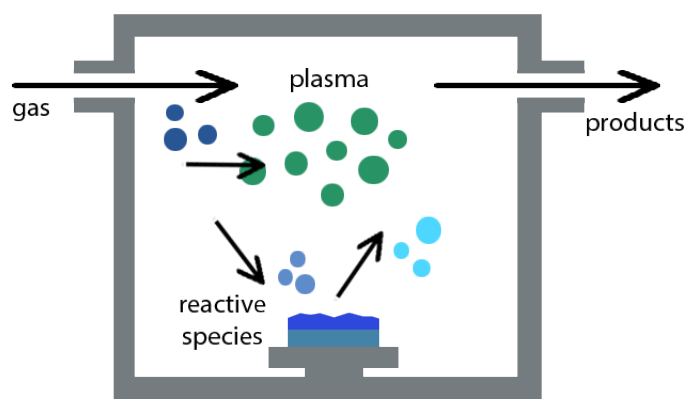


Figure 4.5: PECVD schematic.

The material which is deposited with PECVD is silicon nitride (Si_3N_4) and its main purpose is to insulate the characterization structures (Hall bars, TLM bars) with respect to the remaining zinc phosphide film, allowing a well defined geometry. The Si_3N_4 layers have been deposited at 300 °C and they have a thickness of 30 *nm*. The deposition has been done with an Oxford Plasmalab 100 tool in the EPFL cleanroom in the Physics faculty by R.Paul.

4.1.4 Plasma etching

Plasma etching has been used to remove Si_3N_4 layers from the surface. It is a type of dry etching where the chemical active components are generated by the interaction with plasma in a chamber. Once the reactive species hit the sample, a reaction occurs and the volatile product is removed by a pumping system, leaving the surface etched [40]. Being a dry etching method, it allows anisotropic etching, so a sufficient control of the etching direction. Moreover, it is a method to successfully etch hard dielectrics such as it is Si_3N_4 , which in a wet etch process is mainly attacked by phosphoric acid [41].

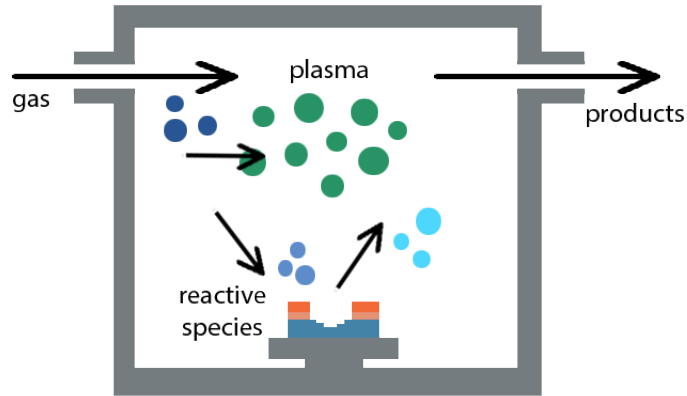


Figure 4.6: Plasma etching chamber schematic.

The machine available in CMI cleanroom (SPTS APS) exploits fluorine chemistry for silicon nitride etching. In particular, the recipe adopted exploits a combination of CHF_3 and SF_6 . The selectivity with respect to the e-beam resist is 2:1. Concerning the etching time, being the dielectric layer about 30 nm thick and the etching time $160\text{-}220 \text{ nm/s}$, the process was set to last maximum 60 seconds [42]. Before to start the effective etching, to clean the chamber avoiding contamination an oxygen cleaning process was run for about 1 minute.

4.1.5 E-beam resist and lift-off

As explained in the dedicated section, to perform e-beam lithography a resist must cover the substrate surface. Different resists show different properties and polarities. In this work a combination of PMMA (poly methyl methacrylate) and MMA (methyl methacrylate) have been adopted, because they are positive resists (e.g. resists becoming soluble when exposed) and ideal for lift-off process. In particular, MMA EL9 and PMMA 495 A4 have been spin-coated with different thicknesses (coater velocity) depending on the e-beam steps [43]: for metal deposition, a combination of MMA ($\sim 440 \text{ nm}$) and PMMA ($\sim 220 \text{ nm}$) was used to perform lift-off, while to carve out Hall and TLM bars from the silicon nitride layer only PMMA ($\sim 120 \text{ nm}$) has been used. After resist coating, the sample was heated at $180 \text{ }^\circ\text{C}$ for 5 minutes to improve resist adhesion. To develop the resists, the sample was dipped into MiBK:IPA 1:3 (1 min) and IPA (1 min).

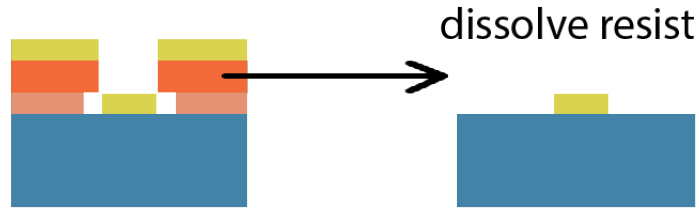


Figure 4.7: Lift off process

Concerning lift-off, it is a technique which has the advantage to save one etching step after a deposition: when a layer is deposited on top of a patterned resist sufficient thicker than the layer to deposit, if the undercut after development is big enough the deposited layer will not be continuous between the region where it fills the pattern and the ones on top of the resist. After deposition one can dissolve the resist directly removing the unwanted material [44], as shown in fig. 4.7.

In the case of PMMA and MMA, if one deposits MMA and then PMMA on top, a large undercut can be achieved: being PMMA the polymeric version of MMA, the MMA will be attack easily by the remover for the same exposure. As a remover, acetone was used.

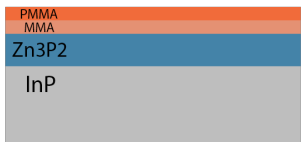
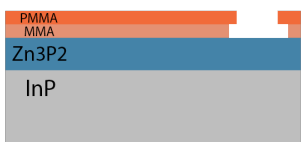
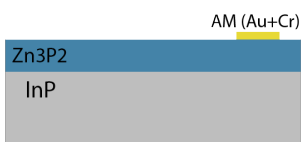
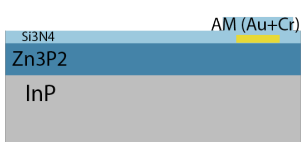
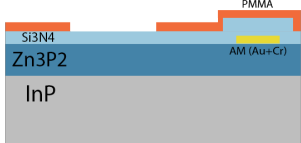
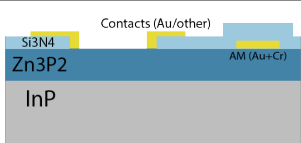
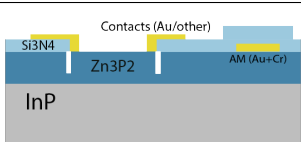
4.1.6 Focused ion beam

Focused ion beam (FIB) machine is a tool allowing characterization, material deposition and milling. The working principle is similar to the SEM, whose details are reported in the appendix.

After finishing the fabrication process, FIB has been used to mill the borders of Hall and TLM bars in order to better define the field lines, "cutting away" the zinc phosphide. This process is possible thanks to ions that are generated by means of an ion gun or exploiting plasma generation [45]. Once high energy-ions hit the substrate, they are able to remove material from the surface. This step was performed using Helios G4 PFIB UXe (xenon ions) machine in CIME facility in EPFL by R. Paul.

4.2 Process flow and structures description

4.2.1 Hall and TLM structures process flow

step	picture
<p>1.1 Spin coating MMA (2000 rpm, 440 nm) + 5min baking 180°C</p> <p>1.2 Spin coating PMMA (2000 rpm, 220 nm) + 5min baking 180°C</p>	
<p>2.1 E-beam lithography (alignment markers)</p> <p>2.2 Development in MiBK:IPA 1:3 (1min) + IPA (1min)</p>	
<p>3.1 Cr/Pt (10 nm) + Au (100 nm) sputtering with DP-650</p> <p>3.2 Lift-off in acetone</p>	
<p>4.1 PCVD of Si₃N₄ (30 nm) to create an isolating layer</p>	
<p>5.1 Spin coating PMMA (6000 rpm, 120 nm) + 5min baking 180°C</p> <p>5.2 Repeat steps 2.1 and 2.2 (Hall and TLM bars)</p>	
<p>6.1 Plasma etching of Si₃N₄ (O₂ cleaning 60 sec + 45-60 sec etching)</p> <p>6.2 Resist strip in acetone</p>	
<p>7.1 Repeat steps 1.1 - 2.2 for the contacts</p> <p>7.2 Au (100-150 nm) sputtering with DP-650</p> <p>7.3 Lift off in acetone</p>	
<p>8.1 FIB milling</p>	

4.2.2 CV pads and junction pads process flow

step	picture
<p>1.1 Spin coating MMA (2000 rpm, 440 nm) + 5min baking 180°C</p> <p>1.2 Spin coating PMMA (2000 rpm, 220 nm) + 5min baking 180°C</p>	
<p>2.1 E-beam lithography (alignment markers and ohmic pads)</p> <p>2.2 Development in MiBK 1:3 (1min) + IPA (1min)</p>	
<p>3.1 Au (100-150 nm) sputtering with DP-650</p> <p>3.2 Lift-off in acetone</p>	
<p>4.1 Repeat steps 1.1 - 2.2 for the Schottky contacts</p> <p>4.2 Schottky metal sputtering with DP-650</p> <p>4.3 Lift off in acetone</p>	
<p>5.1 Bond a Au-covered wafer with silverpaste for junction capacitance measure</p>	

4.2.3 Fabricated structures

In the previous sections the steps and the process flows have been described. In the following subsections the resulting structures will be visually presented. In fig.4.8 the TLM structures (A and B) can be observed. The presence of the silicon nitride surrounding the bar in structure A (left in the picture) can be noticed looking at the different colour of the bar with respect to the surroundings.

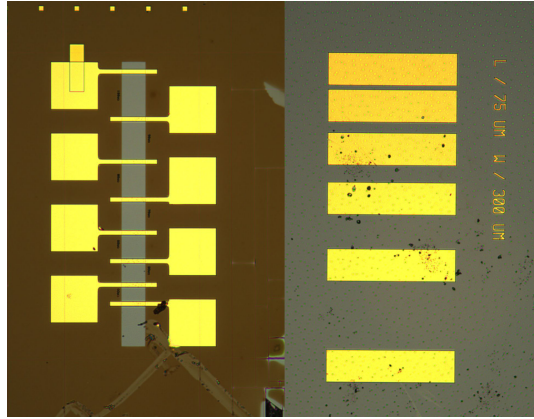


Figure 4.8: TLM structure version A (left) and B (right).

In the case of the structure A, the device for TLM has been defined by multiple e-beam lithography steps to pattern the silicon nitride and deposit the contact, while the structure B was made with one e-beam step only (stopped at the point 3.2 of the process flow).

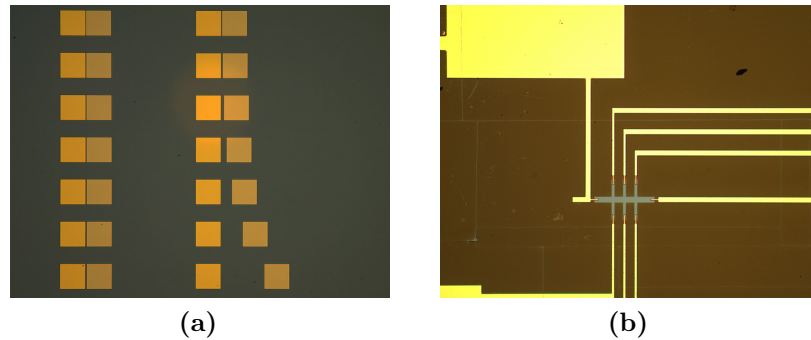


Figure 4.9: C-V pads (a) and Hall bar (b) structures.

Picture 4.9 shows the structure of the different C-V pads. The yellow pads are the ohmic ones, while the gray pads are the Schottky contacts. The other figure is a picture of a Hall bar. As it can be seen, there are quite big pads: the reason is related to the risk of delamination during wire bonding and, as a consequence, the creation of open circuits between the bar and the pads. To avoid this possibility, big multiple pads have been placed around the normal pads of the bar.

Chapter 5

Results

In these sections the results of the electrical characterization performed on several Zn_3P_2 on InP thin films is presented. The strategy is to start characterizing the thin films at the micro-scale with traditional TLM measurements and C-V profiling to extract resistivity from the TLM, carrier concentration from C-V and then the hole mobility combining the different data. Afterwards, the $\text{Zn}_3\text{P}_2/\text{InP}$ junction is analyzed looking at the threshold and the diode ideality factor. Finally, everything is put in correlation with the composition data obtained from the SIMS analysis. TLM measurements show that the doping of the substrate has a significant impact on the possibility to probe Zn_3P_2 . Therefore, the results obtained with this technique were used to guide the following characterization steps. Hall measurements will be discussed in the Appendix, as the results obtained from this kind on technique are not perfectly exhaustive.

Overall, the results of this characterization analysis give a general understanding of the main electrical properties of Zn_3P_2 thin films for solar cell devices.

5.1 TLM measurements

TLM measurements have been the starting point of the analysis. The voltage range was set from -500 mV to +500 mV. The samples used are monocrystalline on n-type InP, p-type InP and intrinsic, polycrystalline on intrinsic InP. Depending on the kind of substrate different behaviours have been observed: plotting the resistance versus the length it is possible to see a straight line, scattered points or lines with different slopes. A similar behaviour is reflected in the I-V curves, which in some cases appeared ohmic for certain length ranges, to finally acquire Schottky characteristics. These behaviours are related to the substrate: following the supplier data, doped InP shows a carrier concentration of about 10^{18} cm^{-3} , which corresponds to a resistivity around $10^{-3} \Omega \cdot \text{cm}$ or $10^{-2} \Omega \cdot \text{cm}$ depending if it is

n-type of p-type; this means that current could flow across the $\text{Zn}_3\text{P}_2/\text{InP}$ interface depending on the distance between the contacts and the Zn_3P_2 resistivity. In this process the band alignment between material and substrate plays an important role: despite comparable or lower resistivity values of the substrate, an unfavorable band alignment will result in an high equivalent junction resistance, impeding the carriers to cross the barrier.

5.1.1 Monocrystalline Zn_3P_2 on n-type InP

The monocrystalline films on n-type substrate analyzed are samples 17B (Au contacts) and 17C (Ag and Au contacts). Their TLM graphs are shown in fig. 5.1. As it can be observed, their behaviour is similar and the resistances measured are comparable in magnitude (few $\text{M}\Omega$). Data points for 17C (Ag) appears more scattered and a data cleaning process has been performed on it. The difference is probably due to the presence of slightly superficial cracks.

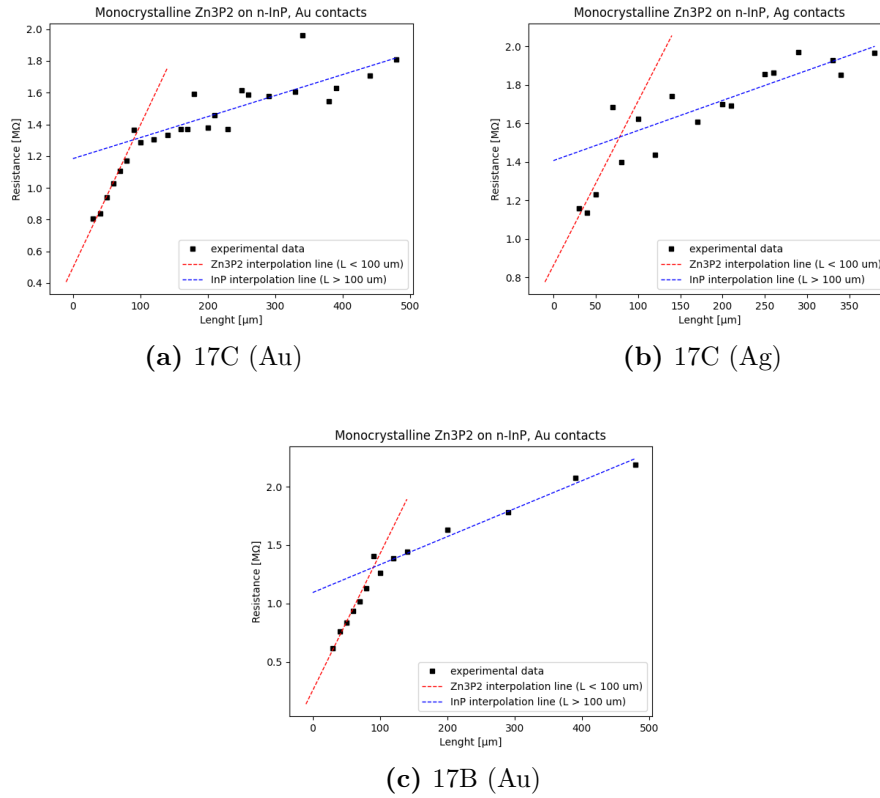


Figure 5.1: Resistance versus length for monocrystalline on n-type InP samples. Black markers show the acquired data.

A double slope is present for a length of about $100 \mu m$ (L_{crit}). The first line (red in the figure) is the interpolation line related to zinc phosphide, while the second one (blue) takes into account the contribution of indium phosphide and the junction at the interface: in fact, one can consider that if the distance between the pad is smaller than L_{crit} the current is totally flowing in Zn_3P_2 . For higher distances, the resistance offered by the junction and the InP path is lower than the Zn_3P_2 one, allowing the current to flow across the junction.

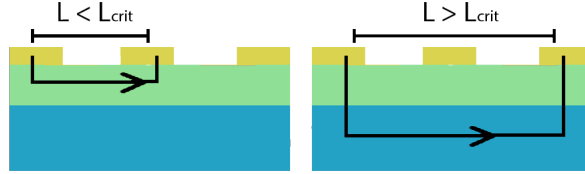


Figure 5.2: Different current paths depending on the length.

An evidence of the barrier crossing is given by the I-V curves: as reported in fig 5.3, gradually increasing the distance between the pads the behavior passes from ohmic to Schottky and this is observed for all the samples. Moreover, the shape of the Schottky curves, bended for both positive and negative voltages, could be an indication of a double crossing of the barrier, meaning the current crosses the interface to flow in InP and then it crosses it again to come back towards the contact.

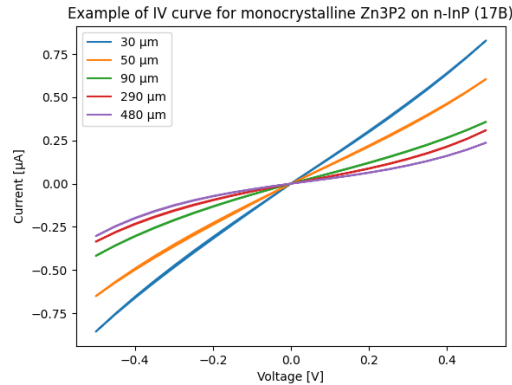


Figure 5.3: Example of I-V curves for 17B sample. The curves are ohmic for small distances and then they become Schottky. The picture reports the behaviour until L_{crit} and for the maximum distance ($480 \mu m$).

The relevant data can be extracted from the first slope of the TLM curves in fig. 5.1. The average resistivity for this kind of samples is $(46.37 \pm 4.68) \Omega \cdot cm$. The values

related to the contact resistance and the contact resistivity appear more scattered, though they are of the same order of magnitude. The reason of this difference is probably related to the presence of the junction with the InP, which could lead to a non-exact estimation of the values. Concerning the transfer length, $L_T > L_{contact}$ in all the cases. This could be influenced either by the presence of the junction, either by the remaining zinc phosphide native oxide or silicon nitride under the contact, which could lead to a spread of the field lines. Table 5.1 summarizes the data. One notices that the high errors for 17C (Ag) are due to the high scattering between the points.

sample	Resistivity ($\Omega \cdot cm$)	Contact resistance ($k\Omega$)	Contact resistivity ($\Omega \cdot cm^2$)	Transfer length (μm)
17C (Au)	44.9±3.7	248.2±23.7	3.4±1.9	27.6±4.9
17C (Ag)	42.6±19.8	431.2±113.1	10.9±8.8	50.6±36.8
17B (Au)	51.6±5.0	110.7±31.5	0.6±0.3	10.7±4.1

Table 5.1: Summary of TLM data from monocrystalline on n-type samples.

Concerning the band alignment with n-InP, in fig. 5.4 there is the related COMSOL Multiphysics simulation. One should notice that the potential barrier made by the built-in potential and the bands mismatch seems to be high, around 0.8-1 V. Actually, as it will be described in the next sections, monocrystalline on n-InP samples exhibit the lower diode threshold, indicating that the real barrier is smaller than the one computed with the tool.

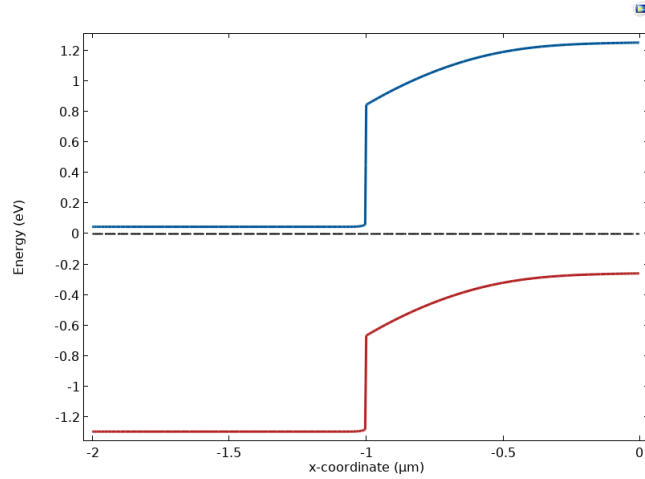
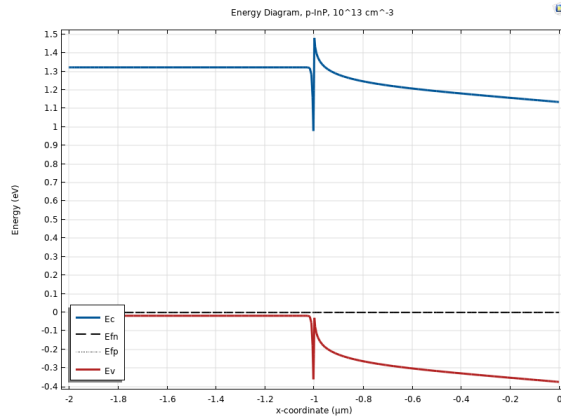


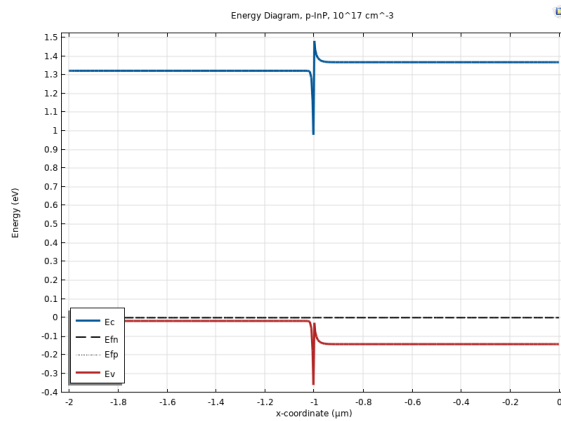
Figure 5.4: Band alignment for Zn_3P_2 (right) and n-InP (left). Zinc phosphide carrier concentration was set to $10^{15} cm^{-3}$.

5.1.2 Monocrystalline Zn₃P₂ on p-type InP

Concerning the samples on p-type substrate, if one consider that zinc phosphide is intrinsically p-type, the band alignment with InP could result in a shallow junction, depending on the carrier concentration of the film. Given the supplier data for the substrate, an approximated band alignment can be computed.



(a) Zn₃P₂ carrier concentration: 10^{13} cm^{-3}



(b) Zn₃P₂ carrier concentration: 10^{17} cm^{-3}

Figure 5.5: Band alignment for InP (left in the graph) and Zn₃P₂ (right in the graph). The thickness of the region featuring barriers at the interface is about 80-50 nm, while the barrier height is 0.2-0.1 eV, depending on the chosen carrier concentration.

Fig 5.5 shows the simulated bands by means of COMSOL Multiphysics using the 1D semiconductor module: the carrier concentration for Zn₃P₂ was varied from a minimum of 10^{13} cm^{-3} to a maximum of 10^{17} cm^{-3} and in each case the junction appears shallow.

A shallow junction along with the low resistivity of doped InP suggests that $L_{crit_{p-sub}} \ll L_{crit_{n-sub}} \approx 100 \mu m$. This means that the current is able to flow directly into the substrate even for short distances, thus the zinc phosphide contribution could be masked. Fig.5.6 shows the I-V curves and the TLM plot for sample 06C (monocrystalline, Au contacts) using the configuration B of TLM structure.

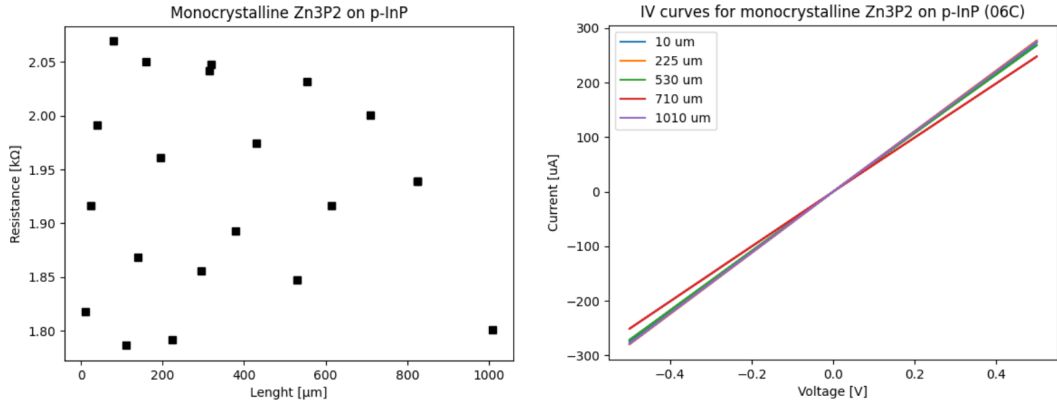


Figure 5.6: TLM graph (left) clearly shows the scattered behaviour, while the I-V curves (right) remain perfectly ohmic for a large distance range.

As it can be observed, the resistance values are scattered, comprised between $1.8 k\Omega$ and $2 k\Omega$. These values are mainly related to the contact contribution and no relevant information about zinc phosphide can be extracted. Looking at the I-V curves, they appear ohmic even for long distances: this is explained by the presence of the shallow junction. Due to this behavior, samples on p-type substrate have been scarcely considered for the following analysis.

5.1.3 Polycrystalline and monocrystalline Zn₃P₂ on i-InP

The behavior of the samples grown on intrinsic InP is quite different, since for the investigated lengths no double slopes or scattered points have been observed. This could be due to a combination of the higher resistivity of the InP and the resistance offered by the junction, which are favoring the flow of current through Zn₃P₂ entirely. Fig.5.7 shows the TLM graphs for the same polycrystalline sample (04C) with different metals as contacts. As it can be seen, the points lay on the same interpolation line, meaning the conduction is mainly through zinc phosphide.

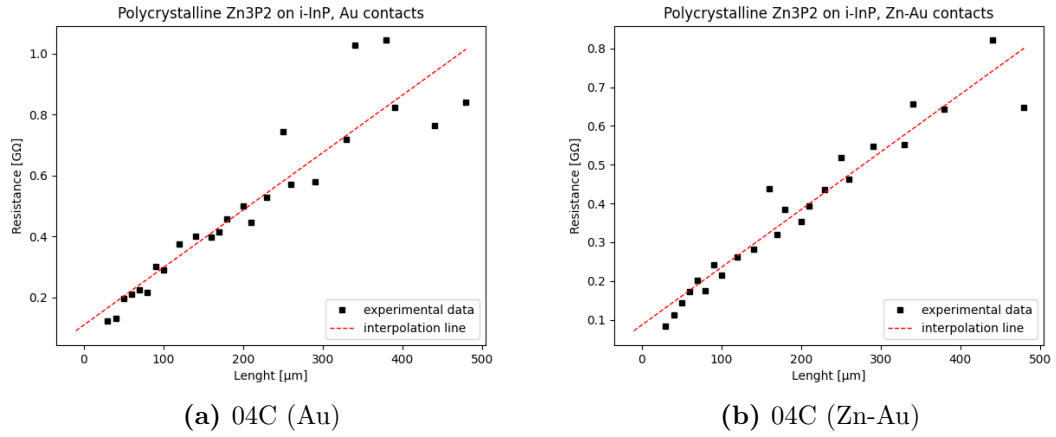


Figure 5.7: TLM graphs for polycrystalline samples with different metal contacts.

TLM are lateral measurements, which means that the current flows crossing the grain boundaries leading to higher resistivity. In particular, the obtained resistivity is $(8.43 \pm 1.40) \text{ k}\Omega \cdot \text{cm}$. Grain boundaries have an effect also on the contact parameters, which are much higher with respect to monocrystalline samples. Concerning the I-V curves, given the resistance in the range of $\text{G}\Omega$ the current values are affected by a significant noise. Nonetheless, it is still possible to recognize an ohmic behaviour meaning there is no junction effect. Fig. 5.8 shows some examples of I-V curves.

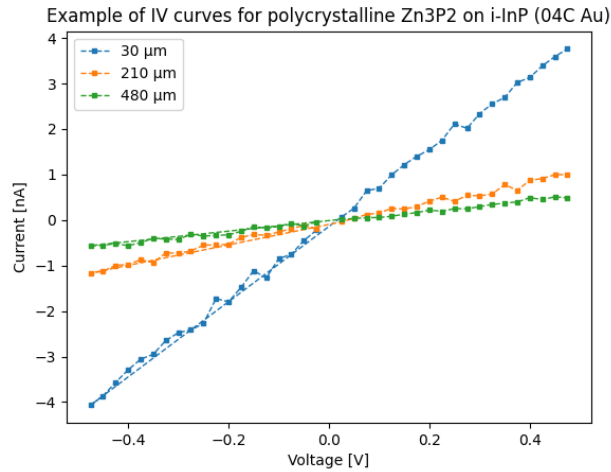


Figure 5.8: Example of I-V curves for 04C (Au) sample. The curves are slightly noisy, but ohmic.

A similar behavior was found also for one of the monocrystalline samples on intrinsic InP. Similarly to the samples featuring an n-type substrate, the resistivity is much lower with respect to the polycrystalline samples, hitting $154.6 \Omega \cdot cm$. The contact parameters are of the same order of magnitude of the ones registered for 17B (Au) and 17C (Au). For what concerns the transfer length, the value is 78.3% of the physical contact length. Table 5.2 summarizes the extracted parameters while fig. 5.9 shows the I-V curves and TLM graph.

sample	Resistivity ($\Omega \cdot cm$)	Contact resistance ($k\Omega$)	Contact resistivity ($\Omega \cdot cm^2$)	Transfer length (μm)
04A (Au)	154.6 ± 10.7	242.3 ± 25.9	0.95 ± 0.4	7.83 ± 1.4

Table 5.2: Summary of TLM data from 04A sample.

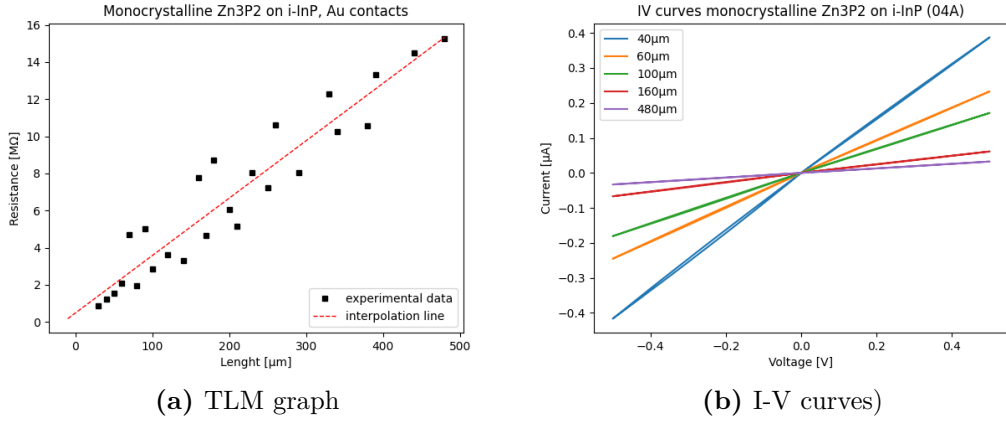


Figure 5.9: TLM graph and I-V curves for monocrystalline sample (04A) on intrinsic indium phosphide substrate.

The other monocrystalline film on which TLM measurements have been performed is V1-19-02-11-A. Unfortunately, for this sample the points were quite scattered and extracting a resistivity value could lead to a non-indifferent error. Also in this case it is useful to simulate the band alignment to observe what is the behavior of the junction. Fig. 5.10 shows that it is similar to the one of the n-InP, though the depletion region in the InP is larger thanks to the small doping.

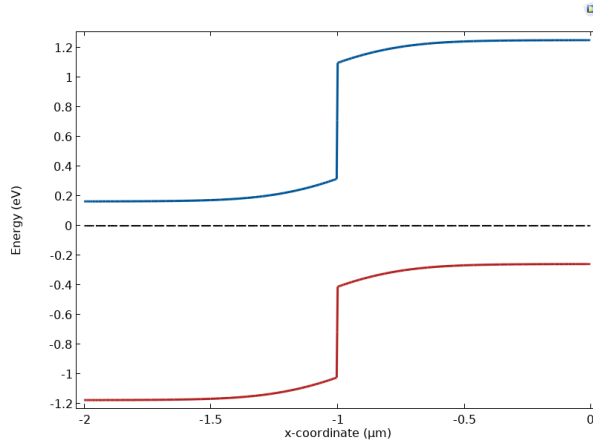


Figure 5.10: Band alignment for Zn_3P_2 (right) and i-InP (left). Zinc phosphide carrier concentration was set to 10^{15} cm^{-3} .

Among the different metals for the contacts, the most used one was gold: it is able to form a good ohmic contact with zinc phosphide and it was the only metal always available in the sputtering system. Table 5.3 reports the contact data related to gold on monocrystalline Zn_3P_2 :

sample	Contact resistance ($k\Omega$)	Contact resistivity ($\Omega \cdot \text{cm}^2$)
17B (n-InP)	110.7	0.6
17C (n-InP)	248.2	3.4
04A (i-InP)	242.3	0.95

Table 5.3: Summary of Au contact parameters for monocrystalline zinc phosphide.

The average contact resistance is $(200.4 \pm 77.7) \text{ k}\Omega$, while the contact resistivity shows more variation, being $(1.65 \pm 1.53) \Omega \cdot \text{cm}^2$. These variations could be due to the presence of the InP junction, which could slightly alter the slope of the first line: if this does not heavily change the contact resistance (found from the intercept with the R-axis), it impacts more on the contact resistivity, being proportional to the square of the transfer length (found from the intercept with the L-axis). Nonetheless, overall the values show good agreement, meaning that the substrate has a limited influence: this is in agreement with the hypothesis of the current flowing in zinc phosphide only.

One can note that there is a big difference between the contact resistances listed in the table and the resistance measured for the sample with a p-type substrate, which was around $2 \text{ k}\Omega$. The TLM bar used for the p-type sample has been underposed on a different kind of process, where only one e-beam step was done, without

depositing Si_3N_4 . The different surface treatment, as well the milling time with Argon during contact deposition, could be the principal causes of the discrepancy.

5.2 C-V profiling

The mobility μ can be computed starting from the carrier concentration N and the resistivity of the sample ρ by means of $1/\rho = q\mu N$. So, the purpose of C-V profiling is to find the carrier concentration to obtain a mobility value.

Given the results of the TLM analysis, the main samples on which C-V has been performed are the monocrystalline films on n-InP and i-InP and the polycrystalline ones on i-InP. The DC voltage range was set from -2V to 2V for measurements on Schottky diodes, while the AC signal had a frequency of 1-2 MHz with an amplitude of 30-50 mV. The frequency was set to have the maximum signal to noise ratio. For C-V performed to analyse the $\text{Zn}_3\text{P}_2/\text{InP}$ junction the DC and AC parameters were strictly related to the individual sample. As convention, all the data will be plotted considering a bias applied to the Zn_3P_2 region, regardless the structure type.

5.2.1 C-V profiling of Schottky diodes

Following the chapters 2 and 4, Schottky diodes have been realized in a planar configuration, with the Schottky contacts placed at different distances with respect to the ohmic ones and made of different metals. The distance of the contacts and the metal type should have a minor impact on the estimated carrier concentration itself. Nonetheless, their influence on the series resistance and the barrier height can affect the quality of the measurements: high leakage results in a high dissipation factor, which is translated into a less trustworthy measure [46].

Metal whose workfunction respects the constraints to create a depletion region with Zn_3P_2 are for example Al, Cr, Ti, Mg or Fe. Fig. 5.11 shows the comparison between the I-V curves of Schottky diodes realized with different metal contacts available in the sputtering system (Al, Cr, Ti), for the same distance between the pads ($2 \mu\text{m}$) and the same polycrystalline on intrinsic InP sample (06B): chromium seems to be the worst choice in terms of leakage, while titanium is the one providing a good rectifying behavior along with small leakage. Nonetheless, it must be said that the contact quality has found to be quite related to the process, so in the following analysis both Ti and Al will be used as well, also due to the scarce availability of Ti in the sputtering system.

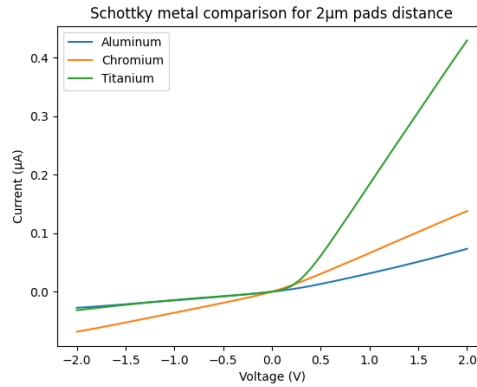


Figure 5.11: I-V comparison for Al, Cr, Ti.

As mentioned, the kind of metal does not heavily affect the carrier concentration that can be extracted from the slope of the C-V curves: an example is shown in fig. 5.12, where it can be seen that the order of magnitude is the same. In particular, an average made on the metal types for 2 μm pad distance gives a carrier concentration of $(5.06 \pm 2.53) \times 10^{13} \text{ cm}^{-3}$. Moreover, in all the cases the lines are decreasing (depletion region increasing for negative voltages), which in accordance with the chosen convention for the bias means the semiconductor is a p-type, as expected from Zn_3P_2 .

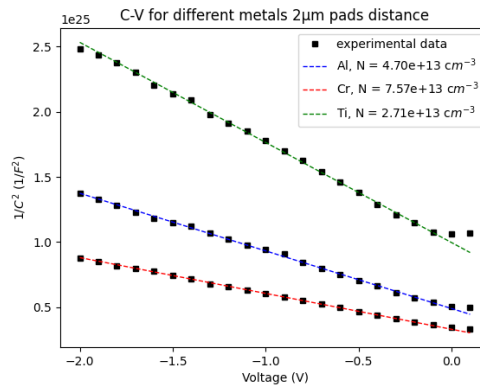


Figure 5.12: C-V comparison for Al, Cr, Ti.

The pads are placed at different distances on the surface. Following the TLM discussion, this means that there is the chance for the current to flow in the substrate, crossing the junction. In chapter 2 the effect of the junction on the depletion capacitance was analyzed, showing that for a given frequency it should

not have a significant impact on the total measured capacitance. If one measures the intersection with the voltage axis of the $1/C^2$ interpolation line, the value of the voltage where the intersection happens is related to the value of the built-in potential: if the junction has an active role, the intersection point should change significantly with respect to the distance. Fig. 5.13 shows normalized intersection points taken between $16 \mu m$ and $128 \mu m$ for a monocrystalline sample on n-InP: TLM suggested a barrier crossing around $100 \mu m$, but it can be observed that minor changes in the intersection occur ($|\Delta V_{max}| \sim 0.1 \text{ V}$), meaning that the effect of the junction can be effectively neglected.

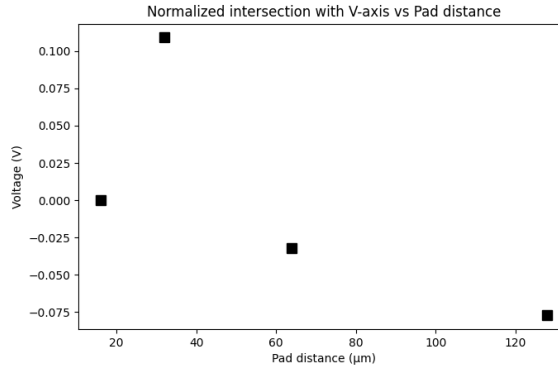


Figure 5.13: Intersection points with the voltage axis for monocrystalline Zn_3P_2 on n-InP. The values have been normalized with respect to the first point.

Concerning the effect of the distance on the extracted carrier concentration, small variations have been observed in the slopes of the $1/C^2 - V$ curves. Nonetheless, the maximum variation coefficient registered is less than 25% when computing the carrier concentration for different samples and for pads distance in various ranges. For example, fig. 5.14 shows some $1/C^2 - V$ interpolation lines for sample V1-19-04-06-B (polycrystalline on i-InP) for Ti and Al: as it can be observed, regardless the metal and the distance the carrier concentration belongs to the same order of magnitude. So, in the following only few curves per samples will be reported. If present in the pictures, the variation coefficient is the total one computed on all the pads distances.

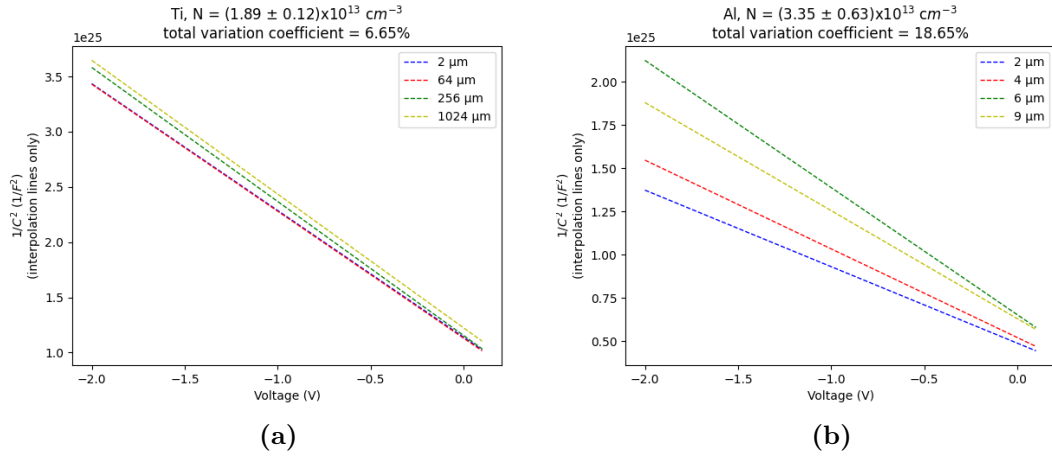


Figure 5.14: Some interpolation lines for sample V1-19-04-06-B extracted for different pad distances and metal. The graphs report the registered variation coefficient between the lines and the computed carrier concentration.

Polycrystalline Zn_3P_2

The polycrystalline films on intrinsic indium phosphide samples investigated are V1-19-10-29-A (Al, Cr), V1-19-04-06-B (Al, Cr, Ti) and V1-19-04-04-C (Ti). Fig. 5.15 shows a comparison between 10-29-A and 04-06-B using Cr and Al as metal and for a fixed pad distance:

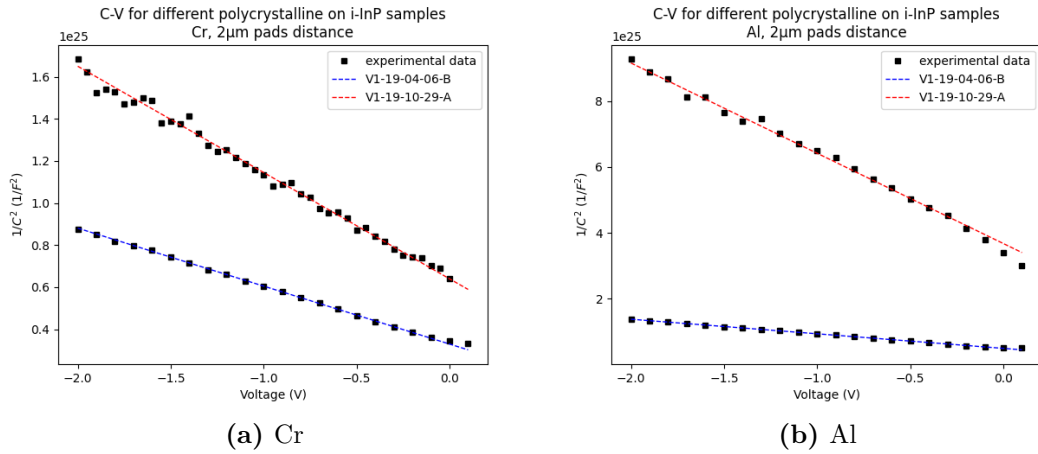


Figure 5.15: Comparison between two polycrystalline on intrinsic substrate (V1-19-10-29-A, V1-19-04-06-B) for Cr and Al contacts.

Despite the chromium curves have a comparable slope, indicating a similar composition between the samples, the ones for aluminum are different. If one computes the carrier concentration for sample V1-19-10-29-A (Al) its range is 10^{12} cm^{-3} , which is at the limit of the detection, so it cannot be considered as a reliable value. Sample V1-19-04-04-C has been investigated using a Ti pad and it is the polycrystalline sample showing the largest variation coefficient. Fig. 5.16 reports a comparison with V1-19-04-06-B for the same metal:

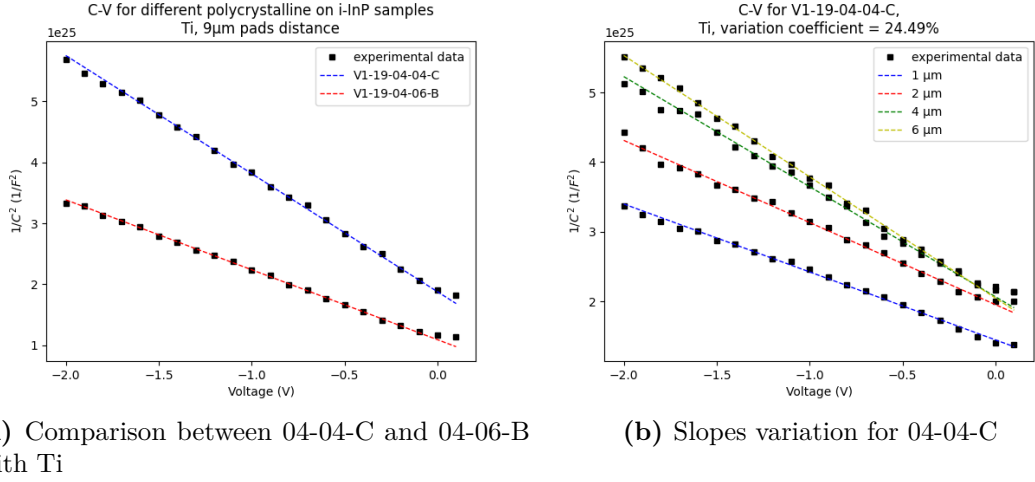


Figure 5.16: 04-04-C comparison with 04-06-B showing a similar carrier concentration (a). A focus on the variation coefficient of 04-04-C (b).

Table 5.5 reports the carrier concentration for all the polycrystalline on intrinsic indium phosphide samples, along with the metal type and the relative uncertainty details. Making an average for V1-19-04-06-B measurements with respect to the values in the table, the carrier concentration results to be $(3.84 \pm 1.71) \times 10^{13} \text{ cm}^{-3}$.

sample	Metal contact	N (cm^{-3})	Variation coefficient
19-10-29-A	Cr	$(4.11 \pm 0.25) \times 10^{13}$	5.95%
19-10-29-A	Al	10^{12} range	-
19-04-04-C	Ti	$(1.40 \pm 0.34) \times 10^{13}$	24.49%
19-04-06-B	Cr	$(6.29 \pm 0.97) \times 10^{13}$	15.34%
19-04-06-B	Al	$(3.35 \pm 0.63) \times 10^{13}$	18.65%
19-04-06-B	Ti	$(1.89 \pm 0.12) \times 10^{13}$	6.65%

Table 5.4: Summary of polycrystalline on i-InP data from C-V profiling with Schottky diodes.

Monocrystalline Zn_3P_2

The monocrystalline samples analyzed are 17A (n-InP substrate) and V1-02-11-A (i-InP substrate). Metals used are Al for 17A and Ti for V1-02-11-A. Figs. 5.17 show the different slopes of the two samples for the same distance range.

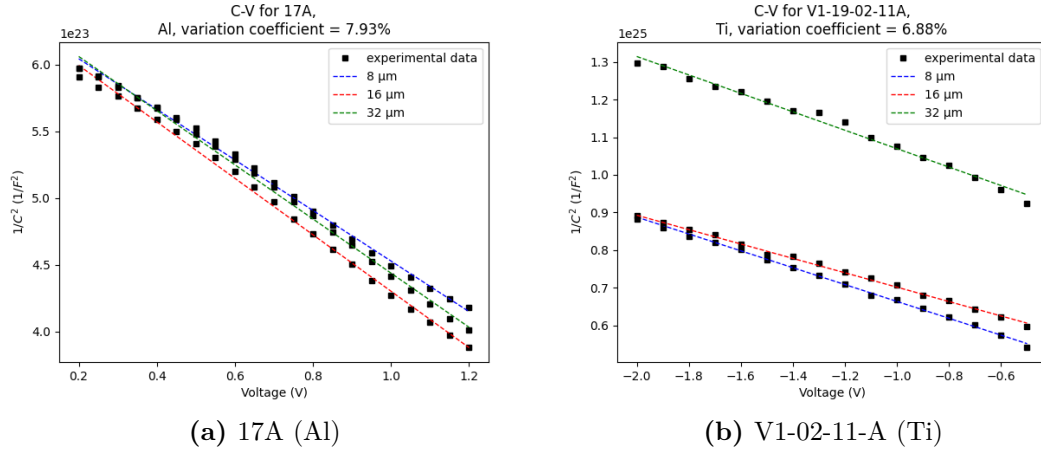


Figure 5.17: C-V profiling for monocrystalline samples 17A (a) V1-02-11-A (b).

It can be noticed the different order of magnitude for the $1/C^2$ axis: 10^{23} for 17A and 10^{25} for the other sample. This difference could be related to an offset, which would explain also the excessively high threshold that the interpolation of the C-V curves for sample 17A seems to suggest. The reason of this offset is hard to determine, because both the samples have been analyzed applying an AC signal with 1 MHz frequency and amplitude of 30-50 mV. One explanation could be the presence of parasitic elements (such as the series resistance) that are changing the transfer function of the total measured capacitance, altering the amplitude of the values one records for a given frequency.

It can be seen that a similar behavior is happening for sample V1-02-11-A: C-V curve for 32 μm appears shifted. Nonetheless, the extracted slope from the fitting is comparable with the ones obtained for the other pads distances, suggesting the presence of local inhomogeneities whose mainly effect on the system is to act on its frequency behavior.

Table 5.5 summarizes the carrier concentration extracted from the two samples:

Sample	Substrate	Metal	N (cm ⁻³)	Variation coefficient
17A	n-InP	Al	$(1.09 \pm 0.08) \times 10^{15}$	5.95%
19-02-11-A	i-InP	Ti	$(1.07 \pm 0.07) \times 10^{14}$	6.88%

Table 5.5: Summary of monocrystalline on i-InP and n-InP data from C-V profiling with Schottky diodes.

5.2.2 C-V profiling of Zn₃P₂/InP junction

At the interface between the film and the substrate a capacitance is formed. Depositing a contact on top of Zn₃P₂ and attaching a gold-covered Si chip at the bottom of InP with silver paste, the analyzer can sense it. Despite the simplicity of this "top-bottom" approach, there are few things to take into account to effectively extract the carrier concentration: the ohmicity of the contact deposited on the film, and the presence of the grains in polycrystalline samples. As it will be shown in the following, if the contact is not ohmic the shape of the C-V curve can change (inverse slope sign), while the grains can lead to a change in the slope, usually resulting in an overestimation of the carrier concentration [47]. Particularly, a huge effect is caused by grains perpendicular to the junction [48], as it is for the available samples. Concerning the C-V profiling with Schottky diodes, this effect seems to have an impact only for frequencies much lower than the one adopted [49].

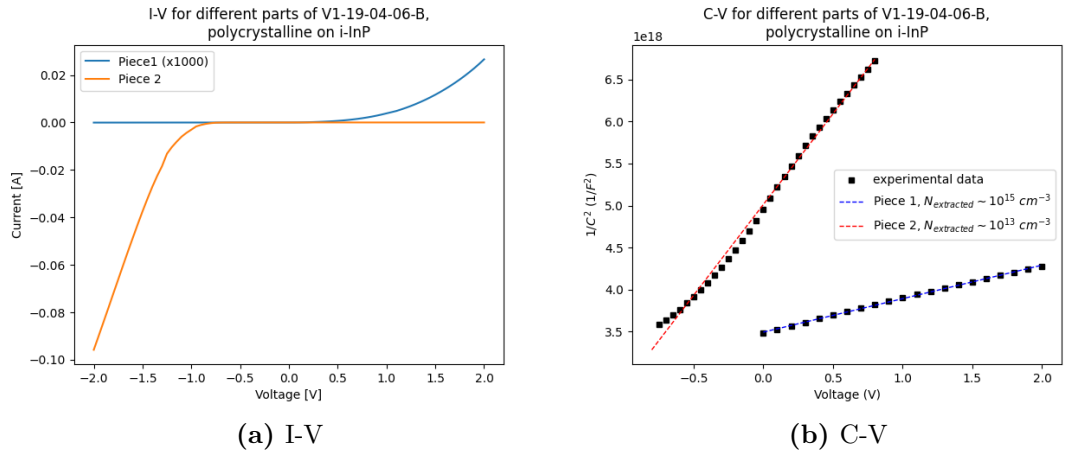


Figure 5.18: I-V curves and C-V profiling for two pieces of V1-19-04-06-B (polycrystalline on i-InP).

Different samples, monocrystalline and polycrystalline on n-type and intrinsic substrates have been analyzed with this technique. Fig. 5.18 reports I-V and

C-V curves for two different pieces of sample V1-19-04-06-B: I-V curve underlines that the contact of the second piece is not ohmic and the Schottky behavior is totally masking the one of the junction (orange curve); for this reason, a Schottky model was applied to extract the carrier concentration. C-V curve instead shows the different slopes of the two curves: from the first piece the extracted carrier concentration is 10^{15} cm^{-3} , which is two order of magnitude higher than the one extracted from the second piece and from the C-V profiling with Schottky diodes. This is related to the effect of the grain boundaries.

One notices that the C-V curve of the first piece was scaled and mirrored with respect to the V-axis to highlight the difference in the slope: the different slope sign is caused by the effect of the Schottky contact, which is behaving like the n-part of an equivalent p-n junction. The ohmicity of the contact seems to be poorly dependent by the piece and most probably is related to process variations which start to have a not negligible impact when the contact area is big enough. Concerning the mismatch into the extracted carrier concentration, the piece-to-piece difference could be linked to the different dimension and position of the grains.

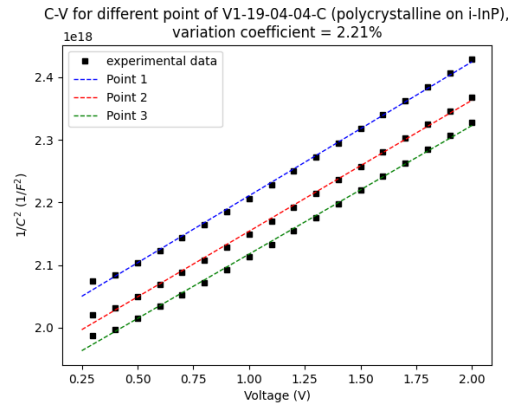


Figure 5.19: C-V profiling for V1-19-04-04-C (polycrystalline on intrinsic InP).

A similar behavior has been found also for sample V1-19-04-04-C, always polycrystalline on i-InP: from the top-bottom C-V profiling the extracted carrier concentration is 10^{15} cm^{-3} , while from the C-V with the Schottky diode it was 10^{13} cm^{-3} . In the section dedicated to SIMS analysis it will appear clear that also in this case there is an overestimation of two orders of magnitude. The slope sign is positive due to the non-perfect ohmic contact.

Concerning the monocrystalline samples, fig. 5.20 reports the I-V and C-V curves for V1-19-02-11-A: also in this case the Schottky behavior can be observed from the I-V curve and the sign of the slope in the C-V curves. Nonetheless, the extracted carrier concentration is $(1.27 \pm 0.01) \times 10^{14} \text{ cm}^{-3}$, in good agreement with the

one extracted using the other C-V method, thanks to the absence of the grain boundaries.

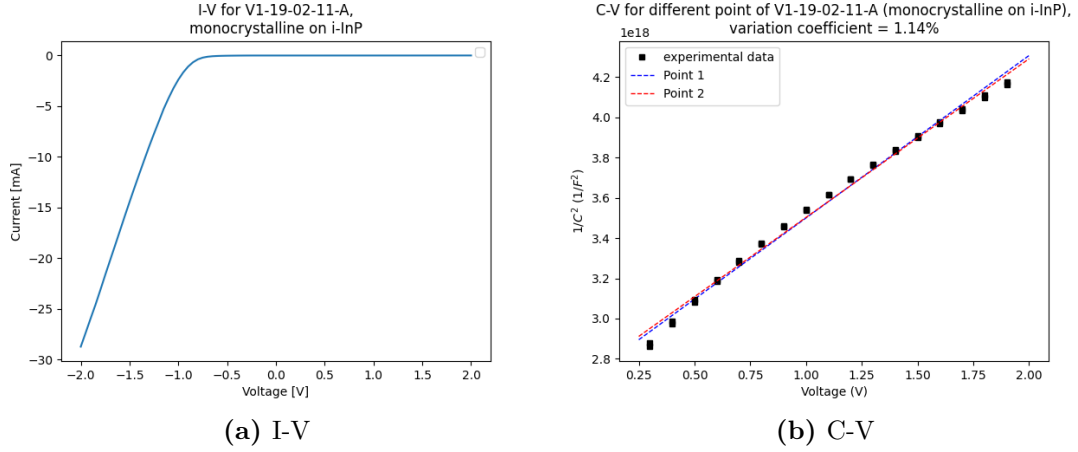


Figure 5.20: I-V and C-V curves for V1-19-02-11-A (monocrystalline on i-InP).

Lastly, two different pieces of V1-19-04-04-A and sample 17C have been analyzed. For example, V1-19-04-04-A films are always monocrystalline on intrinsic substrate. As shown in fig. 5.21, the slope is slightly different, leading to a small variation in the extracted carrier concentration. Averaging on both the data, the carrier concentration for V1-19-04-04-A can be estimated as $(4.03 \pm 0.17) \times 10^{15} \text{ cm}^{-3}$. Also in this case, the Schottky behavior is predominant, leading to a different slope sign.

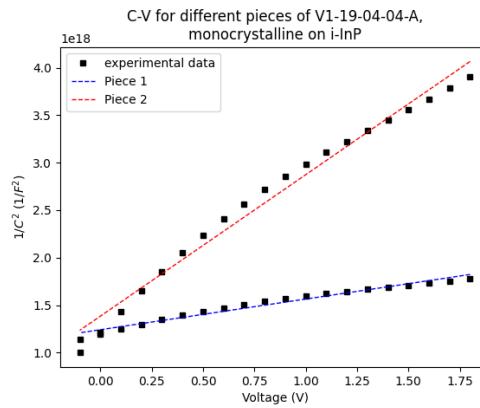


Figure 5.21: C-V profiling for two pieces of V1-19-04-04-A (monocrystalline on intrinsic InP).

Table 5.6 summarizes the data extracted from C-V profiling with the top-bottom method for all the samples except V1-19-04-06-B, whose carrier concentration in the following will be considered to be the average extracted from the lateral measurements.

sample	type	substrate	N (cm^{-3})
19-04-04-C	polycrystalline	i-InP	$10^{15} \Rightarrow 10^{13}$
19-02-11-A	monocrystalline	i-InP	$(1.27 \pm 0.01) \times 10^{14} \text{ cm}^{-3}$
19-04-04-A	monocrystalline	i-InP	$(4.03 \pm 0.17) \times 10^{15} \text{ cm}^{-3}$
17C	monocrystalline	n-InP	$(4.0 \pm 0.13) \times 10^{15} \text{ cm}^{-3}$

Table 5.6: Summary of data from C-V profiling with the top-bottom approach.

5.3 I-V curves comparison, threshold and η

In the previous sections the importance of the the junction between Zn_3P_2 and InP was enlightened. To better understand how the junction is working and what are the differences with respect to the expected behavior, it is useful to plot the I-V curves for each sample typology: polycrystalline and monocrystalline on i-InP, monocrystalline on p-InP and n-InP. The I-V curves have been taken exploiting a top-bottom configuration, with a $150 \mu\text{m} \times 150 \mu\text{m}$ gold contact deposited on Zn_3P_2 .

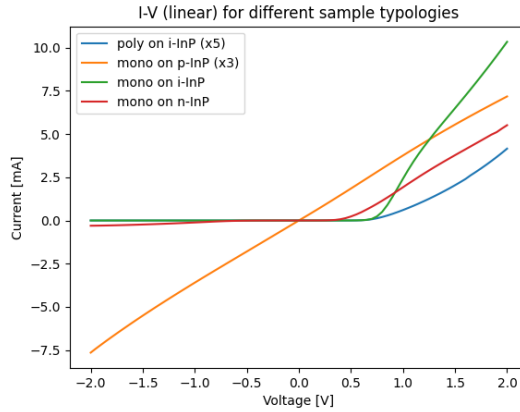


Figure 5.22: I-V in linear scale.

Fig. 5.22 shows the behavior of the I-V curves for the different typologies of the samples: as expected from the results of the previous sections, the monocrystalline

on p-InP is the only one behaving in an ohmic way.

It can be observed that the diodes are not ideal. The changes into the exponential behavior can be well noticed plotting the I-V curve in a semilog scale: different slopes in the linear part of the graph in fig. 5.23 are present.

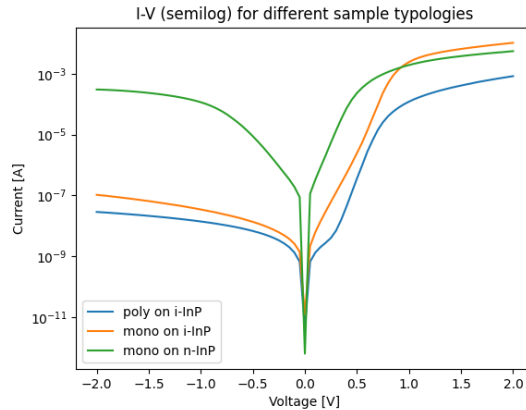


Figure 5.23: I-V in semilog scale.

These regions correspond to different ideality factors η . It is possible to plot the trend of the ideality factor with respect to the voltage to extract useful information about the sample (fig. 5.24): for example, the polycrystalline on intrinsic InP shows a peak in the plot, which can be related to a low shunt resistance, defined as the inverse of the slope of the I-V curve at zero bias [50]. In fact, for low voltages the shunt resistance is the one dominating the η behavior, while for higher voltages the series resistance becomes dominant, causing the growing of η [51].

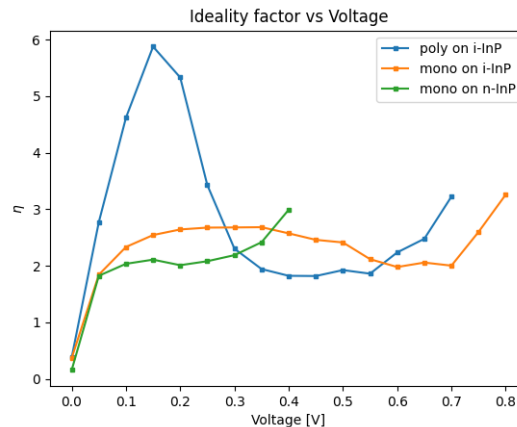


Figure 5.24: Ideality factor vs Voltage.

One can extract the values from the flat part of the ideality factor curves, where the influence of the shunt and series resistances are less relevant. Table 5.24 reports the values along with the carrier concentration of the sample: comparing the monocrystalline films, the one on intrinsic substrate seems to be the most subjected to recombination phenomena. All the samples exhibit a different carrier concentration, that could lead to some variations in term of the ideality factor.

sample	substrate	η	N (cm^{-3})
Polycrystalline	i-InP	1.92 ± 0.03	$\sim 4 \times 10^{13}$
Monocrystalline	i-InP	2.54 ± 0.14	$\sim 10^{14}$
Monocrystalline	n-InP	1.93 ± 0.12	$\sim 4 \times 10^{15}$

Table 5.7: Summary of the ideality factors for the different samples.

In fact, carrier concentration seems to have an impact on the ideality factor, which rises as the carrier concentration increases. An example of this behavior can be observed plotting η trend with respect to the voltage for samples 17A and 17B, both monocrystalline on n-type InP substrate. 17A is the sample previously analyzed ($N \sim 4 \times 10^{15} cm^{-3}$), while 17B has a carrier concentration in the range of $10^{19} cm^{-3}$, as it will be discussed in the next section. As shown in fig. 5.25, 17B exhibits $\eta = 3.46 \pm 0.2$, while 17A has a lower ideality factor, being $\eta = 1.93 \pm 0.12$.

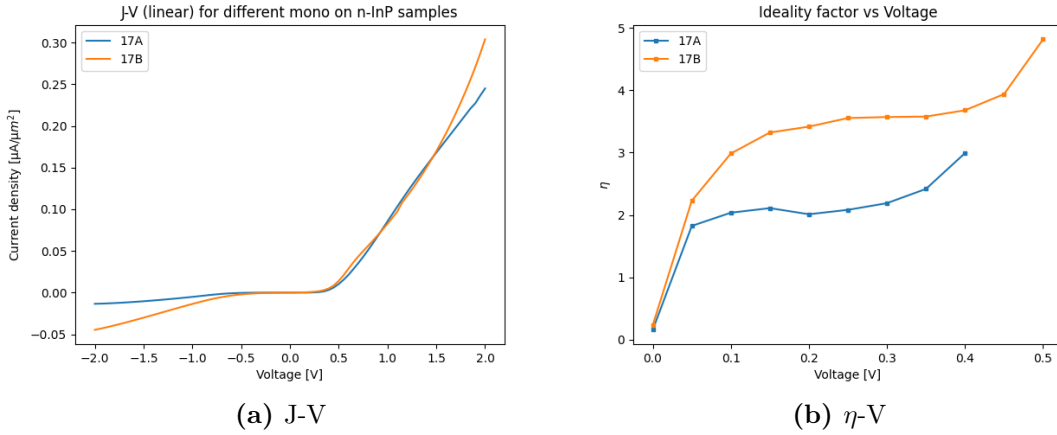


Figure 5.25: I-V and ideality factor curves for 17A and 17B (monocrystalline on n-InP).

Nonetheless, fig.5.25 shows also that the threshold voltage V_{th} of the diode is less affected by the increase of the carrier concentration, despite being related to the built-in potential and so the Fermi level position. Generally, the threshold voltage

can be used as a measure of the "strength" of the junction: as higher is the threshold as difficult will be for the carriers to cross the Zn_3P_2 for a given bias. Threshold values for the different samples typologies are reported in tab. 5.8.

sample	substrate	V_{th} (V)
Polycrystalline	i-InP	~ 0.83
Monocrystalline	i-InP	~ 0.68
Monocrystalline	n-InP	~ 0.47

Table 5.8: Summary of data from C-V profiling with the top-bottom approach.

The low threshold of the monocrystalline films on n-InP is in accordance with what observed from the TLM measurements, where the conduction was happening in the substrate for longer lengths. Concerning the polycrystalline on i-InP, it exhibits a high threshold, which along with the relatively high resistivity of the substrate doesn't allow the current to flow across the junction. Lastly, the monocrystalline on i-InP has a threshold value in the middle: although the film should be less resistive than a polycrystalline one due to the absence of grain boundaries, the lower threshold could still contribute to have a current flow in the substrate: it could be the case of V1-19-02-11-A sample, for which the points appeared scattered tough not as scattered as the monocrystalline sample on p-InP.

5.4 SIMS analysis

Secondary Ion Mass Spectroscopy (SIMS) is a technique used for composition analysis. It exploits a flux of ions (primary ions) bombarding the surface of the sample, which ejects secondary ions. Using a mass spectrometer is then possible to retrieve the relevant information [52]. Some samples have been sent to Eurofin Scientific in U.S.A. to perform this kind of analysis to obtain the Zn and P percentage in the film.

Given the amount of Zn and P in the samples, it is possible to obtain the Zn/P ratio, which gives a fast way to compare different samples. Tab. 5.9 reports sample name and typology, Zn and P amount and Zn/P:

sample	type	Zn atoms/cc	P atoms/cc	Zn/P
17C	mono on n-InP	$(3.57 \pm 0.02) \times 10^{22}$	$(2.42 \pm 0.07) \times 10^{22}$	(1.474 ± 0.05)
17A	mono on n-InP	$(3.60 \pm 0.04) \times 10^{22}$	$(2.40 \pm 0.09) \times 10^{22}$	(1.502 ± 0.08)
02-11-A	mono on i-InP	$(3.67 \pm 0.06) \times 10^{22}$	$(2.32 \pm 0.06) \times 10^{22}$	(1.578 ± 0.07)
04-06-B	poly on i-InP	$(3.73 \pm 0.02) \times 10^{22}$	$(2.27 \pm 0.07) \times 10^{22}$	(1.642 ± 0.06)
04-04-C	poly on i-InP	$(3.70 \pm 0.02) \times 10^{22}$	$(2.30 \pm 0.07) \times 10^{22}$	(1.610 ± 0.06)

Table 5.9: Summary of data extracted from SIMS analysis.

Looking at the Zn/P ratio of samples 04-06-B and 04-04-C with respect to 17A, it is clear that their carrier concentration it is not the same. In particular, being the one of 17A in the order of 10^{15} cm^{-3} , this is a confirmation of the fact that the one of 04-04-C should be of a similar value to the one of 04-06-B, that means around 10^{13} cm^{-3} . Moreover, being 17A stoichiometric one can conclude that the carrier concentration of a perfectly stoichiometric sample is $\sim 10^{15} \text{ cm}^{-3}$.

If one plots the carrier concentration N extracted from C-V profiling with respect to the Zn/P ratio, it is possible to observe a nice exponential trend. Fig. 5.26 shows the points (triangles) and the fitting line (dashed). One can note the presence of V1-19-04-04-A sample also, whose Zn/P ratio (1.469) was obtained from previous Rutherford Backscattering (RBS) composition analysis.

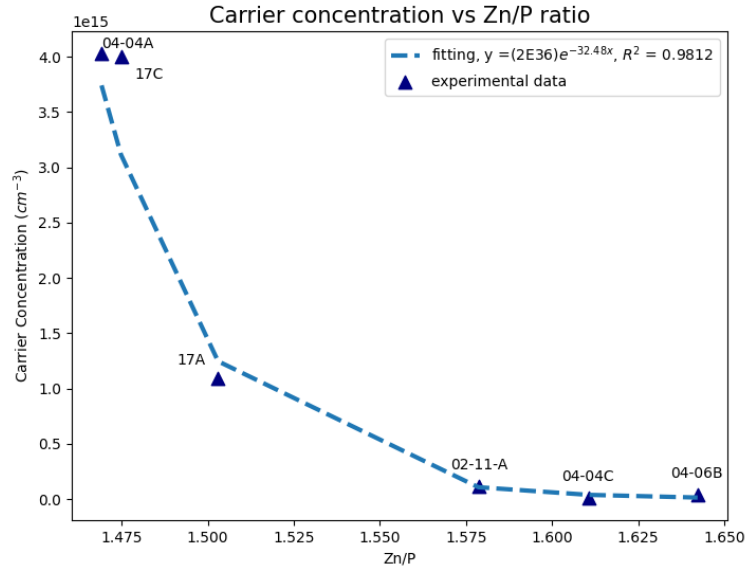


Figure 5.26: Carrier concentration versus Zn/P ratio.

The trend shows that that as higher is the phosphorus concentration (the amount of p-dopants in the crystal) as higher is the carrier concentration. Despite this interesting result, it is possible that the exponential trend is valid only for Zn/P close to the stoichiometric value (1.5): for example, if the concentration of P is too high (low Zn/P ratio) the semiconductor can become degenerated or, maybe, not all the phosphorus atoms will become electrically active. So, in the future would be interesting to analyze samples with a lower Zn/P ratio to observe if a saturation happens. However, starting from the fitting equation and assuming it is valid until degeneration, one can compute what is the minimum Zn/P ratio to have to reach the degeneration point ($E_V = E_F$):

$$N = (2 \times 10^{36}) \times e^{-32.48 \frac{Zn}{P}} = N_V \times e^{\frac{E_V - E_F}{k_B T}} = N_V \quad (5.1)$$

Where N_V is the effective density of states for holes in Zn_3P_2 , k_B is the Boltzmann constant, T is the temperature and E_V and E_F are respectively the valence band and Fermi level values. Using $N_V \sim 2.77 \times 10^{19} \text{ cm}^{-3}$ [53], one can find that to avoid degeneration the following constriction must be respected:

$$\left(\frac{Zn}{P}\right)_{lim} \geq 1.19 \quad (5.2)$$

From previous RBS analys, the Zn/P ratio for sample 17B (monocrystalline on n-InP) results to be 1.165, which is minor than the limit. Extracting its carrier concentration from the interpolation line, one finds that it should be close to $8.5 \times 10^{19} \text{ cm}^{-3}$. To check this, C-V profiling using a top-bottom configuration has been performed:

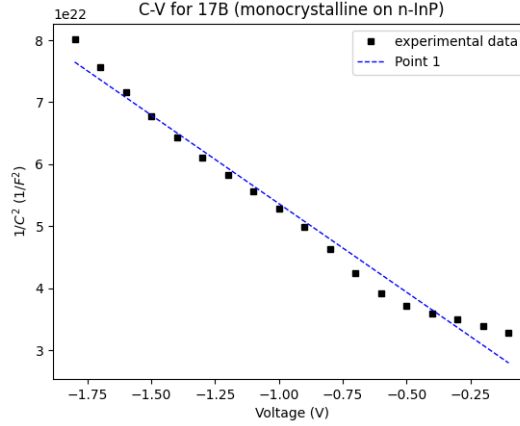


Figure 5.27: C-V profiling for 17B.

The extracted carrier concentration results to be $(1.22 \pm 0.3) \times 10^{19} \text{ cm}^{-3}$, which is slightly less than the value obtained from the fitting. This suggests that the

relation obtained from the fitting is valid, but close to the limit of the Zn/P ratio for the degeneration, the exponential behavior effectively saturates.

5.5 Mobility

Combining all the data from TLM measurements and C-V profiling, the mobility can be finally computed. Both resistivity and carrier concentration play a role into the calculation of μ : grain boundaries, inhomogeneities or a high number of phosphorus interstitials can act as scattering points, decreasing the mobility. For this reason, tab. 5.10 reports a mobility range obtained from the average of the available data for monocrystalline and polycrystalline samples.

type	mobility range cm^2/Vs
Monocrystalline	36-115
Polycrystalline	19-53

Table 5.10: Summary of mobility values.

The mobility of the monocrystalline samples is generally higher, as one could expect from the absence of grain boundaries.

The lowest mobility ($\ll 1 cm^2/Vs$) was achieved for 17B, whose high carrier concentration contribute to increase the scattering. Also for sample V1-19-04-04-A the reported mobility is low ($\sim 10 cm^2/Vs$). Despite being monocrystalline, the low mobility is attributed to the presence of surface states, which are affecting the decay time of the carriers ($\sim 1 ns$) [54]. For this reason, mobility of V1-19-04-04-A was not taken into account to compute the average.

Chapter 6

Conclusions and Outlooks

The purpose of this thesis was to analyze the electrical properties of Zn_3P_2 thin films. The reason behind this project is the lack of literature about this material, whose optical characteristics seem to be extremely promising for cheap but efficient solar cell devices.

To answer this question, the samples have been processed to fabricate test structures. Afterwards, resistivity and contact parameters have been investigated with TLM methods and the carrier concentration was computed starting from C-V profiling results, then compared with the data obtained from SIMS composition analysis. TLM showed the importance of the substrate on the electrical properties of the device. Moreover, with this technique it was demonstrated that Zn_3P_2 thin films grown with MBE exhibit a resistivity of $\sim 50\text{-}150 \text{ }\Omega\cdot\text{cm}$ for almost-stoichiometric monocrystalline films and in the order of $10^3 \text{ }\Omega\cdot\text{cm}$ for more Zn-rich polycrystalline samples.

C-V profiling and SIMS analysis offered a way to link the intrinsic carrier concentration to the Zn/P ratio. In the future, this could be a useful way to engineer the film, changing the growth parameters to target a specific carrier concentration and Fermi level position. Moreover, combining these results with the TLM resistivity one has been able to find a mobility range for both the monocrystalline ($36\text{-}115 \text{ cm}^2/V_s$) and polycrystalline ($19\text{-}53 \text{ cm}^2/V_s$) films.

Concerning the future, it would be interesting to deepen more the relation between the resistivity and the Zn/P ratio, analyzing how differently the resistivity changes for monocrystalline and polycrystalline samples depending on the growth conditions. Also, given the challenges related to the presence of a conductive substrate, it could be useful to grow next Zn_3P_2 films on insulating or semi-insulating material. Nevertheless, this thesis work contributed to the understanding of zinc phosphide thin films electrical properties and their relation with the composition. Along with future investigations, this is a good starting point towards a zinc phosphide solar cell.

Appendix A

Imaging methods

A.1 SEM

Scanning electron microscope (SEM) is one of the most common imaging tool, thanks to the high resolution achieved (up to 1-20 nm) and the possibility to combine the imaging with other characterization methods, such as EDX. The use of electrons is due to their small wavelength λ : following de Broglie relationship ($\lambda \propto \frac{1}{\sqrt{V}}$), higher is the accelerating voltage V of the electrons and lower is their wavelength, resulting in higher resolutions achievable.

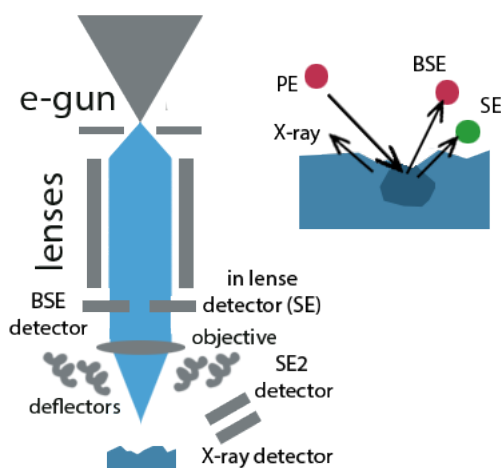


Figure A.1: SEM schematic.

The system consists into a column made up by an electron gun, condenser lenses to

shrink the beam and deflectors and objective lens to deflect and focus the electron flux on the surface. The column is under high vacuum condition to avoid electrons collisions with particles. The gun can be of different types, like a field emission or a thermoionic emission gun, and the voltage range is usually between 0.2-40 kV [55]. Beside the column, the SEM system is equipped with detectors able to capture secondary electrons (SE) and backscattered electrons (BSE). SE have low energy and they are originated from the collision between the surface and the incoming electrons (PE), while BSE are electrons from the beam deflected by elastic scattering interactions with the sample. SE are caught with in lense detector (high resolution) placed perpendicular to the objective and Everhart-Thornley (SE2) detector (topography) placed laterally, BSE detector is placed near the in lense one [56].

The SEM used for the images is the Zeiss Merlin in CIME. It has a field emission gun and it is equipped with detectors for SE (in lense and SE2), BSE and for EDX analysis. EDX technique consists into capturing the x-rays emitted by the sample after beam interaction. Depending on the beam energy it is possible to excite and detect the presence of different elements, reconstructing the composition of the sample [57] [58].

A.2 AFM

A powerful tool to analyze films topography is the atomic force microscopy (AFM). The system uses cantilever with a nano-metric tip radius to contact the surface and register the topography. Depending if the contact is continuous or if the tip oscillates, the AFM operates in contact mode or tapping mode. Tapping mode allows high resolution imaging and reduces the risk to damage the surface with respect to contact mode, so it is the chosen operation for the topography analysis in this work [59].

In tapping mode the cantilever oscillates with a frequency f , which during operation is set to be close to the cantilever resonant frequency $f_0 = \frac{1}{2\pi} \sqrt{\frac{k}{m}}$, with k and m spring constant and mass of the cantilever. The oscillation is caused by piezo-electric elements and depending on how the amplitude of the oscillation A is perturbed the surface can be analyzed. Tip position $z(t)$ is governed by the following equation:

$$m\ddot{z}(t) = -\nu\dot{z}(t) - k(z(t) - z_0) + F(t)_{driving} + F(t)_{tip/sample} \quad (\text{A.1})$$

Where z_0 is the equilibrium position of the tip, $\nu = \frac{2\pi f_0 m}{Q_0}$ is the damping factor, $F_{driving}(t) = Ak \cos 2\pi ft$ is the driving force and $F_{tip-sample}(t)$ is a complex expression representing the interaction between the tip and the sample. Q_0 is the quality factor and it relates the intrinsic cantilever damping with the environment [60].

The signal in tapping mode is the amplitude of the oscillations, directly related to

the tip position. Depending on the surface elements, the oscillation amplitude can be perturbed and so the tip position. An optical element registers the tip position and by means of a feedback system the piezo-motors adjust the driving force to stabilize the oscillation amplitude [61].

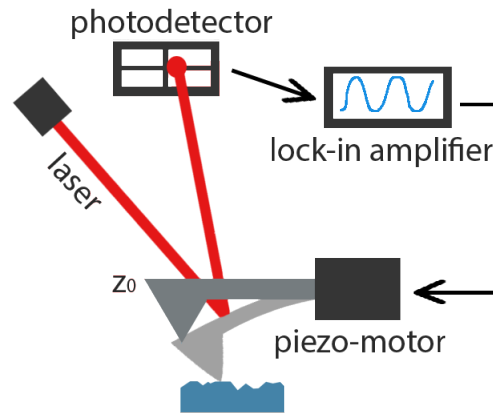


Figure A.2: AFM schematic.

The AFM used is a Cypher S from Oxford Instruments, while the tips are made of platinum silicide. Platinum silicide tips show good mechanical resistance along with high conductivity, making them suitable for conductive AFM (C-AFM) measurements [62]. C-AFM is a technique allowing to measure the electrical response of the sample: while contacting the surface, a bias is applied between the tip and the sample holder and a current is registered [63].

Appendix B

Other results

B.1 Zn_3P_2 on graphene and SiO_2 substrate

This second kind of samples has been grown by R. Paul & co. in LMSC in 2019 by means of Veeco GENxplor MBE reactor. In this case, commercial graphene was used as an intermediate between the grown zinc phosphide and the substrate (300 μm SiO_2 on 100 μm Si) in order to achieve a better material quality by means of van der Waals epitaxy: the absence of dangling bonds in 2-dimensional materials avoids the formation of covalent bonds between zinc phosphide and the underneath graphene, replaced by van der Waals bonds. Thanks to the weakness of these bonds, the epitaxial layer can grow unstrained even with substrates showing 20% of lattice mismatch.

In this case V/II ratio has been varied between 1.3 and 1.7, which has been found to be the optimal range to avoid crystalline Zn formation or material amorphization. Concerning the temperature and the growing time, they play an important role in the surface coverage and film homogeneity, nucleation rate and flakes morphology: it has been observed that growing for 300 minutes at temperature of 150 °C allows the formation of triangular flakes, which will merge creating a film with 101 crystallographic orientation. Also in this case, before to start the growing process, the substrate was subjected to a degassing process at 500 °C for 1 hour [64].

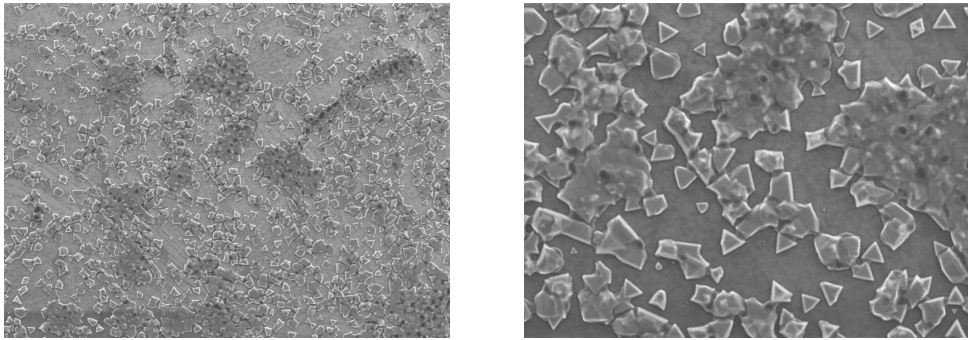
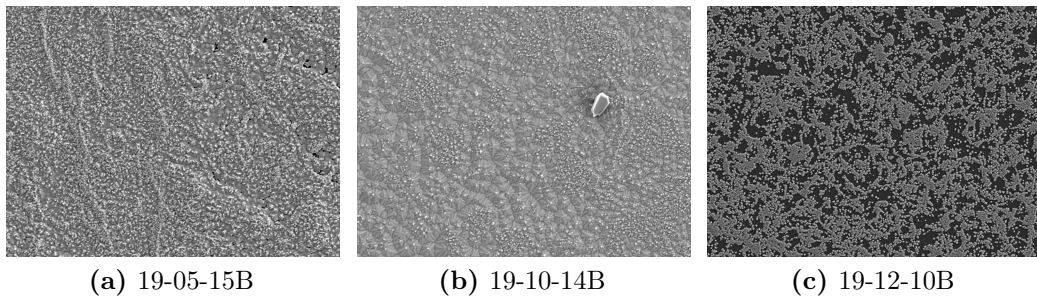


Figure B.1: SEM pictures showing the flakes on the surface (left) and its zoom (right). The dimension of the smaller features is in the range of 100 nm.

With respect to the InP samples, graphene samples show different conditions of the surface: it is sometimes possible to observe the presence of the flakes instead of a homogeneous film (fig. B.1). The different surface conditions is related to the growth parameters (flux ratio, temperature and time of the growth).



(a) 19-05-15B

(b) 19-10-14B

(c) 19-12-10B

Figure B.2: Surface of three different graphene samples.

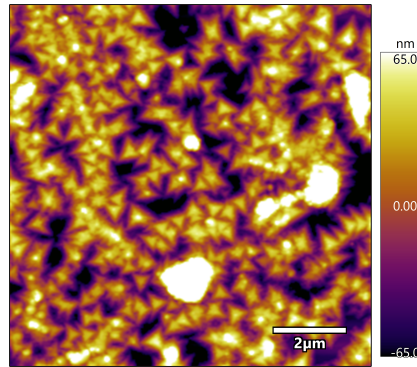


Figure B.3: AFM picture of the sample surface. The presence of isolated triangular flakes is evident.

Lacking of a homogeneous surface coverage, InP samples have been preferred to proceed with the electrical study with respect to graphene samples. Figure B.2 shows different surface conditions highlighting the different film coverage.

B.1.1 EDX

The samples have been analyzed with EDX to obtain info about their composition and to correlate it with the growth parameters. The electron beam was calibrated with a voltage of 4 kV to excite the Zn- $L\alpha$ peak and to retrieve the atomic percentage of the elements composing the film. Besides Zn and P, traces of carbon, oxygen and silicon have been found due to the substrate, but in order to compute the composition ratio their presence has been excluded. In fig.B.4 the composition in atomic percentage of Zn and P has been reported:

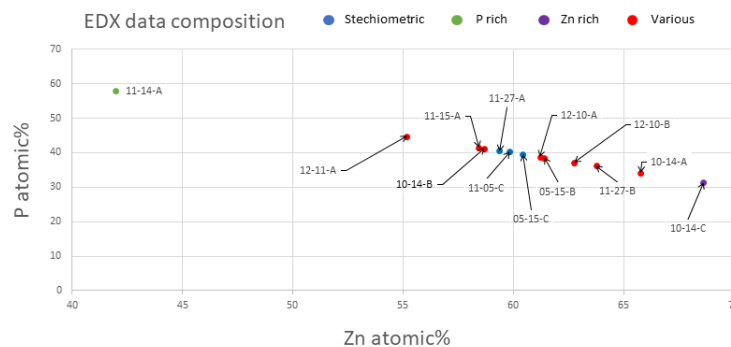


Figure B.4: Composition of the graphene samples in atomic%.

The stoichiometric composition of Zn_3P_2 means a Zn/P ratio of 60:40. In the table below the ratio is reported for each sample. Among all the samples, V1-19-11-14-A and V1-19-10-14-C are respectively the most and less phosphorus-rich, while V1-19-11-05-C, V1-19-11-27-A and V1-19-05-15-C are the most similar ones to the theoretical stoichiometry.

sample	Zn/P
V1-19-05-15-C	1.523
V1-19-12-10-A	1.578
V1-19-11-27-B	1.758
V1-19-10-14-A	1.920
V1-19-10-14-B	1.420
V1-19-10-14-C	2.186
V1-19-05-15-B	1.590
V1-19-11-15-A	1.405
V1-19-11-14-A	0.724
V1-19-12-10-B	1.684
V1-19-12-11-A	1.230
V1-19-11-05-C	1.491
V1-19-11-27-A	1.462

Table B.1: Table showing the Zn/P for the different Zn_3P_2 on graphene samples.

Stoichiometry is dependent by growth parameters, such as molecular flux ratio between Zn and P (II/V) and growth temperature. Fig B.5 reports the stoichiometry with respect to these parameters:

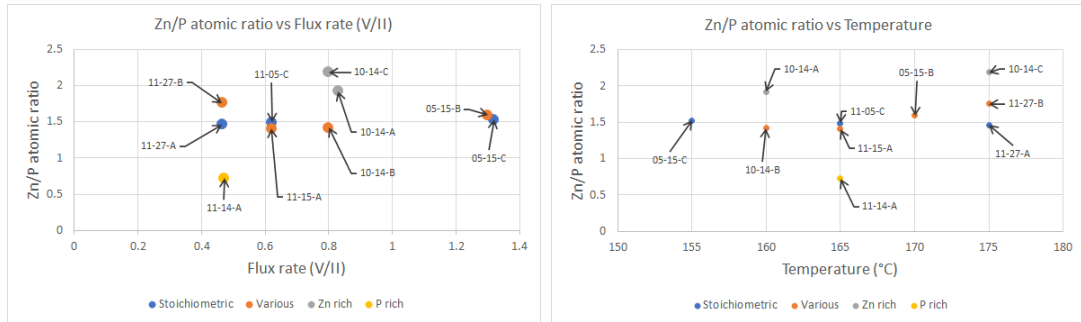


Figure B.5: Zn/P atomic ratio vs gas flux ratio (V/II) in the chamber (left) and growth temperature (right).

As it can be observed, the points appear scattered and there are no particular relations between the Zn/P ratio, the flux and the temperature. An explanation of

correlation lack is related to the small number of available samples, which along with the variations in the conditions of the MBE reactor doesn't allow a profitable statistical analysis.

Nonetheless, R. Paul et al. showed that the flux and the temperature have a huge impact on the morphology: for high flux ratio the Zn_3P_2 flakes on the surface appear as spherical, and they become triangular when decreasing the ratio. Similarly, for temperatures $\leq 100^\circ\text{C}$ the flakes are gathered in clusters, while increasing the temperature they start to become crystalline triangular flakes; then for temperature over 180°C the growth rate starts to decrease due to Zn desorption [64].

B.2 Zn_3P_2 on InP substrate: Hall measurements and transport

Hall measurements are a common method used to extract material parameters such as mobility, resistivity and carrier concentration. The procedure consists into applying a fix current and measuring the resistances value on different channels while sweeping on the values of an applied magnetic field. The current is applied along the "longitudinal channel", while the Hall voltage appears across the "transversal channel". In the next subsections theory and the fabrication process to obtain a sample to do the measures with will be discussed.

B.2.1 Principle

Hall effect [65] consists into the appearance of a voltage V_H when a magnetic field is applied transversely to the direction of charges flux. If current I_x is flowing in x direction and the magnetic field B_z is applied along the z -axis:

$$V_H = \frac{R_{yx}}{I_x} \quad (\text{B.1})$$

Where R_{yx} in equation B.1 is the transversal resistance. From Lorenz force expression in xy -plane, applying B_z in steady state conditions and injecting charge in x direction ($J_y = 0$) results into having the electric field E_y proportional to $B_z \cdot E_x$. So, $V_y = V_H \propto B_z$.

This consideration and eq. B.1 can be used to extract Hall mobility and the carrier concentration. To find their expressions, one can start to write the electric fields expression by means of Ohm's law:

$$\begin{cases} E_x = \rho_{xx}J_x + \rho_{xy}J_y = \rho_{xx}J_x \\ E_y = \rho_{yx}J_x + \rho_{yy}J_y = \rho_{yx}J_x \end{cases} \quad (\text{B.2})$$

With ρ_{xx} and ρ_{yx} longitudinal and transversal resistivity. Following eq. B.1 and the previous considerations, for a fixed current E_y and V_H will only be a function of the magnetic field and the same will be for the transversal resistivity. Combining all together, one can write:

$$\rho_{yx} = \frac{E_y}{J_x} = G \frac{V_H}{I_x} \doteq R_H B_z \quad (\text{B.3})$$

Where G is a geometrical factor and R_H is a proportionality constant known as the Hall coefficient and defined as $R_H = \frac{E_y}{J_x B_z}$. The Hall coefficient is a easy way to measure the coupling between the injection in the x direction and the effect in the y directions thanks to the magnetic field. Knowing that the total resistivity can be expressed as a function of the total carrier concentration N , the scattering time and the effective mass as $\rho_{xx} = \frac{Ne^2\tau}{m}$, one can write:

$$R_H = \frac{E_y}{J_x B_z} = -\frac{1}{Ne} \quad (\text{B.4})$$

This means that R_H can be exploited to recover the carrier concentration. Following the result from equation B.3, R_H is equivalent to the slope of the magneto-resistance line in the transversal channel multiplied by the thickness t of the material:

$$R_H = \frac{R_{yx} t}{B_z} \quad (\text{B.5})$$

The relationships B.4 and B.5 are respectively valid only when there's a dominant type of carriers and the conduction happens in a 3-dimensional space, not involving electrons or holes gases, for which magneto-resistance is subjected to quantization phenomena. When both electrons and holes are present in a similar concentration, R_H becomes dependent by both electrons and holes level and their respective mobility [66].

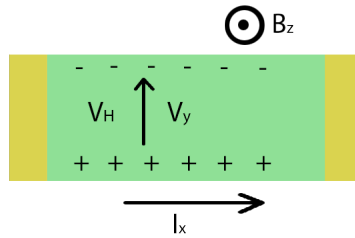


Figure B.6: Appearing of V_H in a p-type semiconductor.

Along with the information obtained by the Hall effect, transport measurements can give more details about the material bandgap: observing the resistivity variations

with temperature across the longitudinal channel, the expected behaviour for a semiconductor material is an exponential increase of the resistivity once the temperature decreases [67]. This can be summarized by the Arrhenius law, considering a room temperature resistivity ρ_0 :

$$\rho = \rho_0 e^{\frac{E_a}{k_B T}} \quad (\text{B.6})$$

Where for low temperatures E_a is the activation energy given by the difference in energy between the relevant band and the acceptors/donors level. Following the expression B.6, it can be extracted from the slope of the resistivity logarithm with respect to $1/T$.

Setup and sample geometry

The setup used for this kind of measurements is a Physical Property Measurement System (PPMS) machine. The tool is able to apply a current and a magnetic field under vacuum, and provides measurements of the resistance across difference channel and for different temperature ranges.

In order to successfully extract R_H and the material parameters, particular sample geometries are exploited: the principal ones are referred as Hall Bar geometry and van der Pauw geometry. They show several pros and cons: the main disadvantage of the Hall Bar geometry with respect to the van der Pauw is the sensitivity of the measure to the geometry, such as the geometrical dimensions of the bar itself or contact misalignment, besides the need to have at least six contacts to apply the current and sense the voltage across the longitudinal and the transversal channel. Nonetheless, van der Pauw geometry requires more time due to the needs to do several measurements to extract the data [68]. For the subsequent measurements, a Hall Bar geometry has been adopted. In the next sections more detailed information about the fabrication method will be given.

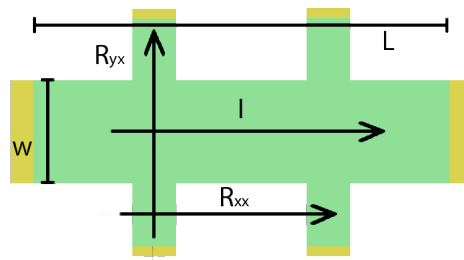


Figure B.7: Structure of a Hall bar showing the current injection and the terminal where the resistances R_{yx} and R_{xx} are sensed.

There are some geometrical constrictions to adopt to minimize the geometry effect on the measurements: length (l) and width (w) are related in order to decrease

the possibility that a too short Hall Bar causes the shortage of the Hall voltage. Maintaining $l \geq 3w$ the error percentage is less than 1% [69].

B.2.2 Results

Hall measurements are a powerful method to extract resistivity, carrier concentration and mobility and in principle it was meant to use this technique to compare the values found from TLM and C-V. Unfortunately, several problems have been encountered, such as the ohmicity and the alignment of the contacts, and few samples have been analyzed. In the following the results for some of these samples will be briefly commented to give a general overview.

The first sample is V1-19-04-06-C, a monocrystalline on p-type substrate. As discussed in the TLM section, the band alignment and the small resistivity of the substrate cause the current to cross the interface between Zn_3P_2 and InP. This can be observed from the Hall measurements also. Fig. B.8 reports R_{xx} versus the temperature (semilog scale). As one can see, the resistance versus temperature shows a mixed behavior, that could be related to carriers crossing the interface. The presence of the peak around 250K is probably related to a fluctuation. Extracting the resistance at room temperature, if one uses the thickness of the InP substrate ($325 \mu\text{m}$) the resistivity is found to be $\rho_{xx} \sim 0.004 \Omega \cdot \text{cm}$, which in the same order of magnitude of the one offered by the wafer.

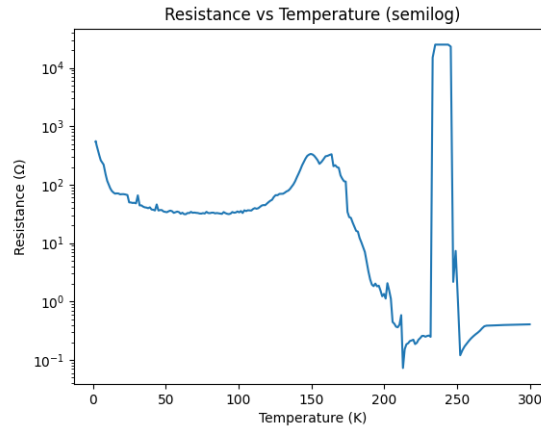


Figure B.8: Resistance versus temperature on the longitudinal channel for a monocrystalline on p-InP.

Another Hall measurement has been performed on a polycrystalline film on intrinsic substrate (V1-19-10-10-A). Fig. B.9 reports the natural logarithm of the resistance across the longitudinal channel versus the inverse of the temperature. From Arrhenius' law the activation energy can be extracted from the slope of the line.

However, the presence of two different slopes suggests the existence of a defect band level.

The extracted activation energies are respectively $E_{a1} \sim 375.5$ meV and $E_{a2} \sim 12.5$ meV. E_{a2} is related to the presence of the mentioned defect level, in accordance with what found by E. Stutz et al, [54], while E_{a1} is the activation energy for conduction.

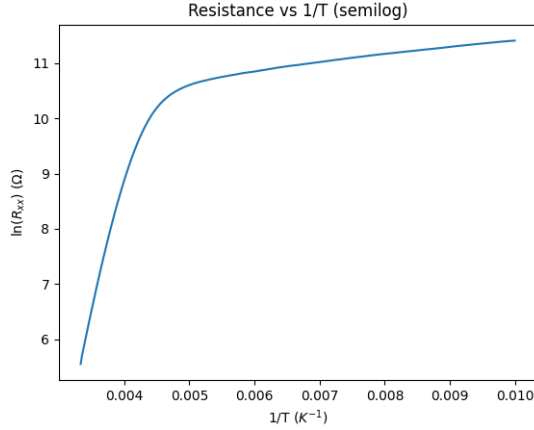


Figure B.9: Natural logarithm of R_{xx} vs $1/T$.

Unfortunately, it was not possible to extract the mobility and the carrier concentration because R_{yx} does not exhibit a linear behavior with the magnetic field. This is mostly related to the effect of R_{xx} variations on R_{yx} when there is a contact misalignment [70]. Fig. B.10 shows the parabolic behavior of R_{xx} .

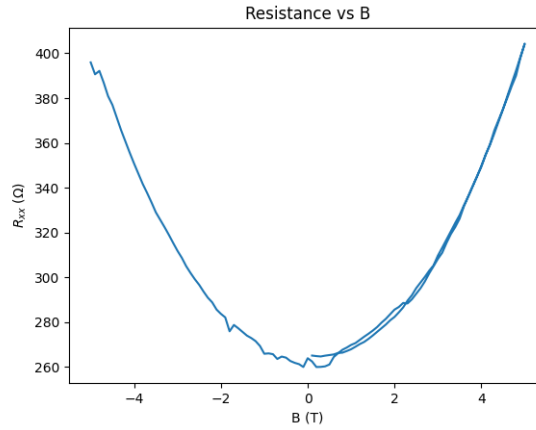


Figure B.10: Parabolic behavior of R_{xx} with the magnetic field.

Hall measurements have been performed also on other kinds of samples, such as 17B (monocrystalline on n-InP). In the case of 17B only resistance fluctuations have been recorded. One plausible explanation is the high carrier concentration, which being close to the degeneration point makes the semiconductor behaving more like a metal. So, also in this case the extraction of the relevant parameters was not possible. Despite the lack of information to compare with the ones illustrated in the previous sections, Hall measurements have been a useful method to give another confirmation to some of the results presented in the previous sections, such as the behavior of the films on p-InP, or in previous studies, such as the presence of the defect band.

Bibliography

- [1] Elias Zsolt Stutz et al. «Stoichiometry modulates the optoelectronic functionality of Zinc Phosphide ($\text{Zn}_{3-x}\text{P}_{2+x}$)». In: *Faraday Discuss.* (2022), pp. -. DOI: 10.1039/D2FD00055E (cit. on p. 1).
- [2] Toshikazu Suda and Kazuhiko Kakishita. «Epitaxial growth of zinc phosphide». In: *Journal of Applied Physics* 71.6 (1992), pp. 3039–3041. DOI: 10.1063/1.350989 (cit. on p. 1).
- [3] M. Bhushan and A. Catalano. «Polycrystalline Zn_3P_2 Schottky barrier solar cells». In: *Applied Physics Letters* 38.1 (1981), pp. 39–41. DOI: 10.1063/1.92124 (cit. on p. 1).
- [4] Jeffrey P. Bosco, Gregory M. Kimball, Nathan S. Lewis, and Harry A. Atwater. «Pseudomorphic growth and strain relaxation of Zn_3P_2 on GaAs(001) by molecular beam epitaxy». In: *Journal of Crystal Growth* 363 (2013), pp. 205–210. ISSN: 0022-0248. DOI: <https://doi.org/10.1016/j.jcrysgro.2012.10.054> (cit. on p. 1).
- [5] Rajrupa Paul et al. «van der Waals Epitaxy of Earth-Abundant Zn_3P_2 on Graphene for Photovoltaics». In: *Crystal Growth & Design* 20.6 (2020), pp. 3816–3825. DOI: 10.1021/acs.cgd.0c00125 (cit. on p. 1).
- [6] Judith Long. «The Growth of Zn_3P_2 by Metalorganic Chemical Vapor Deposition». In: *Journal of The Electrochemical Society* 130.3 (Mar. 1983), pp. 725–728. DOI: 10.1149/1.2119791. URL: <https://doi.org/10.1149/1.2119791> (cit. on p. 1).
- [7] Judith Long. «The Growth of Zn_3P_2 by Metalorganic Chemical Vapor Deposition». In: *Journal of The Electrochemical Society* 130.3 (Mar. 1983), pp. 725–728. DOI: 10.1149/1.2119791 (cit. on p. 1).
- [8] Mischa Flór, Elias Z. Stutz, Santhanu P. Ramanandan, Mahdi Zamani, Rajrupa Paul, Jean-Baptiste Leran, Alexander P. Litvinchuk, Anna Fontcuberta i Morral, and Mirjana Dimitrievska. «Raman tensor of zinc-phosphide (Zn_3P_2): from polarization measurements to simulation of Raman spectra». In: *Phys.*

- Chem. Chem. Phys.* 24 (1 2022), pp. 63–72. DOI: 10.1039/D1CP04322F (cit. on p. 2).
- [9] Steven Demers and Axel van de Walle. «Intrinsic defects and dopability of zinc phosphide». In: *Phys. Rev. B* 85 (19 May 2012), p. 195208. DOI: 10.1103/PhysRevB.85.195208. URL: <https://link.aps.org/doi/10.1103/PhysRevB.85.195208> (cit. on p. 2).
- [10] Wan-Jian Yin and Yanfa Yan. «The electronic properties of point defects in earth-abundant photovoltaic material Zn₃P₂: A hybrid functional method study». In: *Journal of Applied Physics* 113.1 (2013), p. 013708. DOI: 10.1063/1.4772708 (cit. on p. 2).
- [11] M. Bhushan and A. Catalano. «Polycrystalline Zn₃P₂ Schottky barrier solar cells». In: *Applied Physics Letters* 38.1 (1981), pp. 39–41. DOI: 10.1063/1.92124 (cit. on p. 2).
- [12] Alan L. Fahrenbruch Richard H. Bube Faa-Ching Wang. «Electrical properties of Zn₃P₂ single crystals». In: *Journal of Electronic Material* 11 (1982), pp. 75–88. DOI: <https://doi.org/10.1007/BF02654610> (cit. on p. 2).
- [13] Toshikazu Suda and Kazuhiko Kakishita. «Epitaxial growth of zinc phosphide». In: *Journal of Applied Physics* 71.6 (1992), pp. 3039–3041. DOI: 10.1063/1.350989 (cit. on p. 2).
- [14] T. L. Chu, Shirley S. Chu, K. Murthy, E. D. Stokes, and P. E. Russell. «Deposition and properties of zinc phosphide films». In: *Journal of Applied Physics* 54.4 (1983), pp. 2063–2068. DOI: 10.1063/1.332254 (cit. on p. 2).
- [15] A. Haque, T. Dinh, N. Christoforou, D.E. Brodie, and J.D. Leslie. «Preparation and properties of diodes on low-resistivity zinc phosphide films». In: *Thin Solid Films* 176.1 (1989), pp. 13–24. ISSN: 0040-6090. DOI: [https://doi.org/10.1016/0040-6090\(89\)90359-3](https://doi.org/10.1016/0040-6090(89)90359-3) (cit. on p. 2).
- [16] D. Decroix, V. Muñoz, and A. Chevy. «Growth and electrical properties of Zn₃P₂ single crystals and polycrystalline ingots». In: *Journal of Materials Science* 22 (1987). ISSN: 1573-4803. DOI: <https://doi.org/10.1007/BF01233119> (cit. on p. 2).
- [17] Gregory M. Kimball, Nathan S. Lewis, and Harry A. Atwater. «Synthesis and surface chemistry of Zn₃P₂». In: *2008 33rd IEEE Photovoltaic Specialists Conference*. 2008, pp. 1–6. DOI: 10.1109/PVSC.2008.4922747 (cit. on p. 2).
- [18] «Contact Resistance and Schottky Barriers». In: *Semiconductor Material and Device Characterization*. John Wiley Sons, Ltd, 2005. Chap. 3, pp. 127–184. ISBN: 9780471749097. URL: <https://onlinelibrary.wiley.com/doi/abs/10.1002/0471749095.ch3> (cit. on p. 3).

- [19] Sidhant Grover, Shubham Sahu, Peng Zhang, Kristopher O. Davis, and Santosh K Kurinec. «Standardization of Specific Contact Resistivity Measurements using Transmission Line Model (TLM)». In: *2020 IEEE 33rd International Conference on Microelectronic Test Structures (ICMTS)*. 2020, pp. 1–6 (cit. on p. 6).
- [20] Lee Stauffer. *Fundamentals of Semiconductor C-V Measurements*. Accessed: 18-06-2022 (cit. on p. 7).
- [21] M. Bhushan and A. Catalano. «Polycrystalline Zn₃P₂ Schottky barrier solar cells». In: *Applied Physics Letters* 38.1 (1981), pp. 39–41. DOI: 10.1063/1.92124 (cit. on p. 7).
- [22] J.P. Donnelly and A.G. Milnes. «The capacitance of p-n heterojunctions including the effects of interface states». In: *IEEE Transactions on Electron Devices* 14.2 (1967), pp. 63–68. DOI: 10.1109/T-ED.1967.15900 (cit. on p. 10).
- [23] Materials Springer. *zinc phosphide properties*. Accessed: 18-06-2022 (cit. on p. 13).
- [24] N. Convers Wyeth and A. Catalano. «Barrier heights of evaporated metal contacts on Zn₃P₂». In: *Journal of Applied Physics* 51.4 (1980), pp. 2286–2288. DOI: 10.1063/1.327862 (cit. on p. 13).
- [25] Ming-Fu Li and Chih-Tang Sah. «New techniques of capacitance-voltage measurements of semiconductor junctions». In: *Solid-State Electronics* 25.2 (1982), pp. 95–99. ISSN: 0038-1101. DOI: [https://doi.org/10.1016/0038-1101\(82\)90037-5](https://doi.org/10.1016/0038-1101(82)90037-5). URL: <https://www.sciencedirect.com/science/article/pii/0038110182900375> (cit. on p. 13).
- [26] Secondo Franchi. «Chapter 1 - Molecular beam epitaxy: fundamentals, historical background and future prospects». In: *Molecular Beam Epitaxy*. Ed. by Mohamed Henini. Oxford: Elsevier, 2013, pp. 1–46. ISBN: 978-0-12-387839-7. DOI: <https://doi.org/10.1016/B978-0-12-387839-7.00001-4> (cit. on p. 14).
- [27] Simon Escobar Steinvall et al. «Towards defect-free thin films of the earth-abundant absorber zinc phosphide by nanopatterning». In: *Nanoscale Adv.* 3 (2 2021), pp. 326–332. DOI: 10.1039/D0NA00841A (cit. on p. 15).
- [28] Mahdi Zamani, Elias Stutz, Simon Escobar, Reza R Zamani, Rajrupa Paul, Jean-Baptiste Leran, Mirjana Dimitrievska, and Anna Fontcuberta i Morral. «The path towards 1 μ m monocrystalline Zn₃P₂ Films on INP: Substrate preparation, growth conditions and luminescence properties». In: *Journal of Physics: Energy* 3.3 (2021), p. 034011. DOI: 10.1088/2515-7655/abf723 (cit. on p. 15).

- [29] Vladimir G. Dubrovskii, Simon Escobar Steinvall, Virginie de Mestral, Rajrupa Paul, Jean-Baptiste Leran, Mahdi Zamani, Elias Z. Stutz, and Anna Fontcuberta i Morral. «Modeling the Shape Evolution of Selective Area Grown Zn₃P₂ Nanoislands». In: *Crystal Growth & Design* 21.8 (2021), pp. 4732–4737. DOI: 10.1021/acs.cgd.1c00569 (cit. on p. 15).
- [30] V. M. Glazov, A. S. Pashinkin, and L. M. Pavlova. «Thermal Expansion of Gallium and Indium Phosphides: Thermodynamic Evaluation». In: *Inorganic Materials* 37.12 (Dec. 2001), pp. 1207–1215. ISSN: 1608-3172. DOI: 10.1023/A:1012928104121 (cit. on p. 16).
- [31] Judith Long. «The Growth of Zn₃P₂ by Metalorganic Chemical Vapor Deposition». In: *Journal of The Electrochemical Society* 130.3 (Mar. 1983), pp. 725–728. DOI: 10.1149/1.2119791 (cit. on p. 16).
- [32] «12 - Nanofabrication». In: *Nanostructure Control of Materials*. Ed. by R.H.J. Hannink and A.J. Hill. Woodhead Publishing, 2006, pp. 303–330. ISBN: 978-1-85573-933-8. DOI: <https://doi.org/10.1533/9781845691189.30> (cit. on p. 18).
- [33] «Chapter 5 - Manipulation and Patterning of Surfaces (Nanolithography)». In: *Fundamentals and Applications of Nano Silicon in Plasmonics and Fullerenes*. Ed. by Munir Nayfeh. Micro and Nano Technologies. Elsevier, 2018, pp. 89–137. ISBN: 978-0-323-48057-4. DOI: <https://doi.org/10.1016/B978-0-323-48057-4.00005-0> (cit. on p. 18).
- [34] CMI. *Electron beam lithography system*. URL: <https://www.epfl.ch/research/facilities/cmi/equipment/ebeam-lithography/> (visited on 06/22/2022) (cit. on p. 18).
- [35] Jeol. *Thermal emission gun*. URL: [https://www.jeol.co.jp/en/words/emterms/search_result.html?keyword=thermal%5C%20\(thermally%5C%20assisted\)%5C%20field-emission%20electron%20gun](https://www.jeol.co.jp/en/words/emterms/search_result.html?keyword=thermal%5C%20(thermally%5C%20assisted)%5C%20field-emission%20electron%20gun) (visited on 06/22/2022) (cit. on p. 18).
- [36] CMI. *Ebeam - Tool description*. URL: <https://www.epfl.ch/research/facilities/cmi/equipment/ebeam-lithography/raith-ebpg5000/tool-description/> (visited on 06/22/2022) (cit. on p. 18).
- [37] R. Patovan, J. Caro, J. Romijn, and S. Radelaar. «Alignment markers for e-beam writing of the gate level pattern: Fabrication in an intermediate stage and alignment accuracy». In: *Microelectronic Engineering* 6.1 (1987), pp. 117–122. ISSN: 0167-9317. DOI: [https://doi.org/10.1016/0167-9317\(87\)90025-6](https://doi.org/10.1016/0167-9317(87)90025-6) (cit. on p. 19).

- [38] F. Lévy. «Film Growth and Epitaxy: Methods». In: *Reference Module in Materials Science and Materials Engineering*. Elsevier, 2016. ISBN: 978-0-12-803581-8. DOI: <https://doi.org/10.1016/B978-0-12-803581-8.01012-2> (cit. on p. 20).
- [39] Rabindra Satpathy and Venkateswarlu Pamuru. «Chapter 4 - Making of crystalline silicon solar cells». In: *Solar PV Power*. Ed. by Rabindra Satpathy and Venkateswarlu Pamuru. Academic Press, 2021, pp. 71–134. ISBN: 978-0-12-817626-9. DOI: <https://doi.org/10.1016/B978-0-12-817626-9.00004-6> (cit. on p. 20).
- [40] J.H. Wang. «5 - Surface preparation techniques for biomedical applications». In: *Coatings for Biomedical Applications*. Woodhead Publishing, 2017. ISBN: 978-1-84569-568-2. DOI: <https://doi.org/10.1533/9780857093677.1.143> (cit. on p. 21).
- [41] W. van Gelder and V. E. Hauser. «The Etching of Silicon Nitride in Phosphoric Acid with Silicon Dioxide as a Mask». In: *Journal of The Electrochemical Society* 114.8 (), p. 869. DOI: 10.1149/1.2426757 (cit. on p. 21).
- [42] CMI. *SPTS APS*. URL: <https://www.epfl.ch/research/facilities/cmi/equipment/etching/spts-aps/> (visited on 06/23/2022) (cit. on p. 22).
- [43] CMI. *MMA/PMMA resists*. URL: <https://www.epfl.ch/research/facilities/cmi/equipment/ebeam-lithography/raith-ebpg5000/ebeam-resists-available-in-cmi/mma-pmma-resists/> (visited on 06/23/2022) (cit. on p. 22).
- [44] Yifang Chen, Kaiwu Peng, and Zheng Cui. «A lift-off process for high resolution patterns using PMMA/LOR resist stack». In: *Microelectronic Engineering* 73-74 (2004). Micro and Nano Engineering 2003, pp. 278–281. ISSN: 0167-9317. DOI: <https://doi.org/10.1016/j.mee.2004.02.053> (cit. on p. 23).
- [45] T.L. Burnett, R. Kelley, B. Winiarski, L. Contreras, M. Daly, A. Gholinia, M.G. Burke, and P.J. Withers. «Large volume serial section tomography by Xe Plasma FIB dual beam microscopy». In: *Ultramicroscopy* 161 (2016), pp. 119–129. ISSN: 0304-3991. DOI: <https://doi.org/10.1016/j.ultramic.2015.11.001> (cit. on p. 23).
- [46] Jean Carlos Hernandez-Mejia. *Dissipation factor*. URL: https://www.neetrac.gatech.edu/publications/CDFI/6-Tan-Delta-21_with-Copyright.pdf (visited on 07/23/2022) (cit. on p. 36).
- [47] M Amrani, Z Benamara, R Menezla, A Boudissa, M Chellali, T Mohammed Brahim, and F Raoult. «Two-dimensional simulation of the effects of grain boundaries on the C–V characteristics of P+N polysilicon diodes». In: *Journal of Physics D: Applied Physics* 38.4 (Feb. 2005), pp. 596–603. DOI: 10.1088/0022-3727/38/4/012 (cit. on p. 42).

- [48] Jennifer T. Heath, J. David Cohen, and William N. Shafarman. «Bulk and metastable defects in CuIn_{1-x}GaxSe₂ thin films using drive-level capacitance profiling». In: *Journal of Applied Physics* 95.3 (2004), pp. 1000–1010. DOI: 10.1063/1.1633982 (cit. on p. 42).
- [49] C.-M.M. Wu, E.S. Yang, W. Hwang, and H.C. Card. «Grain boundary effects on the electrical behavior of Al-poly-Si Schottky-barrier solar cells». In: *IEEE Transactions on Electron Devices* 27.4 (1980), pp. 687–692. DOI: 10.1109/T-ED.1980.19923 (cit. on p. 42).
- [50] Paul R. Thompson. *METHOD OF MEASURING SHUNT RESISTANCE IN PHOTODIODES*. URL: https://tsapps.nist.gov/publication/get_pdf.cfm?pub_id=841525#:~:text=The%5C%20shunt%5C%20resistance%5C%20is%5C%20defined%2C%20light%5C%20input%5C%20must%5C%20be%5C%20constant. (visited on 08/01/2022) (cit. on p. 46).
- [51] PV Education. *Measuring Ideality Factor*. URL: <https://www.pveducation.org/pvcdrom/characterisation/measuring-ideality-factor> (visited on 08/01/2022) (cit. on p. 46).
- [52] Koralege C. Pathmasiri, Thu T.A. Nguyen, Nigina Khamidova, and Stephanie M. Cologna. «Chapter Ten - Mass spectrometry-based lipid analysis and imaging». In: *New Methods and Sensors for Membrane and Cell Volume Research*. Ed. by Michael A. Model and Irena Levitan. Vol. 88. Current Topics in Membranes. Academic Press, 2021, pp. 315–357. DOI: <https://doi.org/10.1016/bs.ctm.2021.10.005> (cit. on p. 48).
- [53] Springer. *substance: zinc phosphide (Zn₃P₂)*. URL: https://materials.springer.com/googlecdn/assets/sm_lbs/410/sm_lbs_978-3-540-31360-1_273/sm_lbs_978-3-540-31360-1_273.pdf?trackRequired=true&originUrl=/lb/docs/sm_lbs_978-3-540-31360-1_273&componentId=Download%5C%20Chapter (visited on 08/04/2022) (cit. on p. 50).
- [54] Elias Z. Stutz et al. «Showcasing the optical properties of monocrystalline zinc phosphide thin films as an earth-abundant photovoltaic absorber». In: *Mater. Adv.* 3 (2 2022), pp. 1295–1303. DOI: 10.1039/D1MA00922B (cit. on pp. 51, 64).
- [55] Nidhi Raval, Rahul Maheshwari, Dnyaneshwar Kalyane, Susanne R. Youngren-Ortiz, Mahavir B. Chougule, and Rakesh K. Tekade. «Chapter 10 - Importance of Physicochemical Characterization of Nanoparticles in Pharmaceutical Product Development». In: *Basic Fundamentals of Drug Delivery*. Ed. by Rakesh K. Tekade. Advances in Pharmaceutical Product Development and Research. Academic Press, 2019, pp. 369–400. ISBN: 978-0-12-817909-3. DOI: <https://doi.org/10.1016/B978-0-12-817909-3.00010-8> (cit. on p. 54).

- [56] ThermoFisher Scientific. *Electrons in SEM*. URL: <https://www.thermofisher.com/ch/en/home/materials-science/learning-center/applications/sem-electrons.html#:~:text=The%5C%20SE%5C%20detector%5C%20is%5C%20placed,by%5C%20SEM%5C%20users%5C%20for%5C%20imaging>. (visited on 07/12/2022) (cit. on p. 54).
- [57] CIME. *Zeiss Merlin*. URL: <https://www.epfl.ch/research/facilities/cime/electron-microscopy/microscopes/merlin/> (visited on 07/12/2022) (cit. on p. 54).
- [58] CIME. *EDX*. URL: <https://www.epfl.ch/research/facilities/cime/electron-microscopy/introduction-to-em/sem-techniques/edx/> (visited on 07/12/2022) (cit. on p. 54).
- [59] Nader Jalili and Karthik Laxminarayana. «A review of atomic force microscopy imaging systems: application to molecular metrology and biological sciences». In: *Mechatronics* 14.8 (2004), pp. 907–945. ISSN: 0957-4158. DOI: <https://doi.org/10.1016/j.mechatronics.2004.04.005> (cit. on p. 54).
- [60] Hendrik Hölscher. «AFM, Tapping Mode». In: *Encyclopedia of Nanotechnology*. Ed. by Bharat Bhushan. Dordrecht: Springer Netherlands, 2012, pp. 99–99 (cit. on p. 54).
- [61] nanoScience. *Dynamic modes for AFM*. URL: <https://www.nanoscience.com/techniques/atomic-force-microscopy/dynamic-modes-for-afm/> (visited on 07/08/2022) (cit. on p. 55).
- [62] «Chapter 5 - Manipulation and Patterning of Surfaces (Nanolithography)». In: *Fundamentals and Applications of Nano Silicon in Plasmonics and Fullerenes*. Ed. by Munir Nayfeh. Micro and Nano Technologies. Elsevier, 2018, pp. 89–137. ISBN: 978-0-323-48057-4. DOI: <https://doi.org/10.1016/B978-0-323-48057-4.00005-0> (cit. on p. 55).
- [63] Chiara Musumeci, Andrea Liscio, Vincenzo Palermo, and Paolo Samorì. «Electronic characterization of supramolecular materials at the nanoscale by Conductive Atomic Force and Kelvin Probe Force microscopies». In: *Materials Today* 17.10 (2014), pp. 504–517. ISSN: 1369-7021. DOI: <https://doi.org/10.1016/j.mattod.2014.05.010> (cit. on p. 55).
- [64] Rajrupa Paul et al. «van der Waals Epitaxy of Earth-Abundant Zn₃P₂ on Graphene for Photovoltaics». In: *Crystal Growth & Design* 20.6 (2020), pp. 3816–3825. DOI: [10.1021/acs.cgd.0c00125](https://doi.org/10.1021/acs.cgd.0c00125) (cit. on pp. 56, 60).
- [65] Jeffrey Lindemuth. «Hall Effect Measurement Handbook». In: Lake Shore Cryotronics, 2020. ISBN: 1734707801, 9781734707809 (cit. on p. 60).

- [66] «Carrier and Doping Density». In: *Semiconductor Material and Device Characterization*. John Wiley Sons, Ltd, 2005. Chap. 2, pp. 61–125. ISBN: 9780471749097. DOI: <https://doi.org/10.1002/0471749095.ch2> (cit. on p. 61).
- [67] C Hilsum. «Semiconductors (2nd edn)». In: *Physics Bulletin* 30.12 (Dec. 1979), pp. 528–528 (cit. on p. 62).
- [68] Tektronix. *van der Pauw and Hall Voltage Measurements with the 4200A-SCS Parameter Analyzer*. Accessed: 18-06-2022 (cit. on p. 62).
- [69] J. Volger. «Note on the Hall Potential Across an Inhomogeneous Conductor». In: *Phys. Rev.* 79 (6 Sept. 1950), pp. 1023–1024. DOI: 10.1103/PhysRev.79.1023. URL: <https://link.aps.org/doi/10.1103/PhysRev.79.1023> (cit. on p. 63).
- [70] D. Backes, Rhodri Mansell, Martin Lanius, Jörn Kampmeier, David Ritchie, Gregor Mussler, Detlev Grützmacher, and Vijay Narayan. «Disentangling surface and bulk transport in topological insulator p - n junctions». In: *Physical Review B* 96 (May 2016). DOI: 10.1103/PhysRevB.96.125125 (cit. on p. 64).